JGR Space Physics

RESEARCH ARTICLE
10.1029/2023JA032162

Statistical Analysis of Mercury's Magnetotail Lobe Field Using MESSENGER Observations

Charles F. Bowers[1], Caitriona M. Jackman[1], Weijie Sun[2], Mika K. G. Holmberg[1], Xianzhe Jia[3], and Léa Griton[4]

[1]School of Cosmic Physics, DIAS Dunsink Observatory, Dublin Institute for Advanced Studies, Dublin, Ireland, [2]Space Sciences Laboratory, University of California, Berkeley, CA, USA, [3]Department of Climate and Space Sciences and Engineering, University of Michigan, Ann Arbor, MI, USA, [4]LESIA, Observatoire de Paris, Université PSL, CNRS, Sorbonne Université, Université de Paris, Meudon, France

Key Points:

- 1,242 intervals in which Mercury Surface, Space Environment, Geochemistry and Ranging observed the southern lobe of Mercury were identified in 4 years of orbital data
- The lobe field strength (in nT) falls off with distance downtail according to $B_{lobe}(r) = (135 \pm 8) * r^{(-2.1 \pm 0.3)} + (31 \pm 8)$
- Orbit-to-orbit variability in lobe field strength is directly attributable to changing upstream solar wind dynamic pressure

Correspondence to:
C. F. Bowers,
cbowers@cp.dias.ie

Citation:
Bowers, C. F., Jackman, C. M., Sun, W., Holmberg, M. K. G., Jia, X., & Griton, L. (2024). Statistical analysis of Mercury's magnetotail lobe field using MESSENGER observations. *Journal of Geophysical Research: Space Physics*, *129*, e2023JA032162. https://doi.org/10.1029/2023JA032162

Received 10 OCT 2023
Accepted 17 JAN 2024

© 2024. American Geophysical Union. All Rights Reserved.

Abstract The magnetotail lobe region at Mercury is characterized by low plasma density and low magnetic field variability compared to the nightside magnetosheath and central plasma sheet. At Mercury, as well as other planets, lobe magnetic fields play a crucial role in storing and releasing magnetic flux in response to changing upstream solar wind conditions such as interplanetary magnetic field (IMF) orientation and solar wind dynamic pressure (P_{dyn}). This makes the region significant for studying the magnetospheric interaction with the intense solar wind conditions at Mercury's orbit. Here, we identify and analyze magnetotail lobe observations made by the Mercury Surface, Space Environment, Geochemistry and Ranging (MESSENGER) spacecraft during its 4 years orbital phase. We empirically determined a set of criteria using magnetometer (MAG) and the Fast Imaging Plasma Spectrometer instruments onboard MESSENGER to identify lobe magnetic field intervals. From 3,332 MESSENGER orbits, we identify 1,242 lobe field intervals. We derive an expression for the average lobe magnetic field strength in nanotesla with respect to radial distance downtail: $B_{lobe}(r) = (135 \pm 8) * r^{(-2.1 \pm 0.3)} + (31 \pm 8)$. The lobe magnetic field exhibits both small-scale (~3 min) and orbit-to-orbit (~8–12 hr) variability in magnetic field strength compared to this averaged field strength expression. The orbit-to-orbit variability in lobe field strength is not significantly correlated with estimated IMF orientation, but is directly correlated with P_{dyn}. Thus, our findings provide evidence for the pressure balance between the inward facing P_{dyn} on the nightside magnetopause and the outward facing magnetic pressure supplied by the lobes.

Plain Language Summary Of all the planets in the Solar System, Mercury orbits closest to the Sun. As a result, it is subjected to an extreme interplanetary environment driven by solar dynamics. One consequence of the electro-magnetic interaction of the Sun and Mercury is the formation of the magnetotail, which is the result of magnetic field lines connected to the planet being dragged toward the nightside. A portion of the magnetotail, known as the lobe, is characterized by a relative lack of plasma density compared to the surrounding environment. The strength of the magnetic field in the lobe is directly correlated with the conditions in the interplanetary space surrounding Mercury, making it an important region to study the response of a planetary environment to the extreme conditions at Mercury's orbit. We identify and analyze times in which the Mercury Surface, Space Environment, Geochemistry and Ranging spacecraft observed this important region of Mercury's plasma environment. We find direct evidence for the magnetic field lobe's response to the plasma properties emanating from the Sun.

1. Introduction

The magnetotail of Mercury forms as magnetic field lines are stretched downstream by the solar wind, which emanates radially outward from the Sun (Russell et al., 1988). Typically, the magnetotail is comprised of a central plasma sheet characterized by high plasma β (i.e., ratio between the thermal and magnetic pressure), flanked by a northern and southern magnetotail lobe. The magnetotail lobes typically exhibit low plasma β and low fluctuating magnetic field strength compared to the surrounding magnetosheath and plasma sheet. Lobe magnetic field strength responds to changes in upstream solar wind conditions and magnetospheric flux content, making the lobe an important region for analyzing the dynamics of the solar wind magnetospheric interaction at a planet. Given the dominating influence of the solar wind on Mercury's dynamics (e.g., DiBraccio et al., 2013; He et al., 2017; James et al., 2017; Slavin et al., 2010; Sun et al., 2020, 2022), an analysis of the lobe magnetic field is vital for understanding the magnetospheric response to such intense drivers.

At Earth, variations in the rate of dayside magnetic reconnection and upstream solar wind dynamic pressure impact the magnetic flux contained within the lobe (Collier et al., 1998; Fairfield & Jones, 1996; Nakai et al., 1991; Petrinec & Russell, 1996). On the dayside, magnetic reconnection generates open magnetic field lines that stretch from the planet to the interplanetary magnetic field (IMF). These open field lines are then transported to the nightside, populating the lobe and increasing magnetic flux. Subsequent reconnection in the tail closes this flux, completing the Dungey cycle with a typical timescale of 2–3 hr at Earth (Caan et al., 1973; Slavin et al., 1992, 2003). Additionally, an enhancement in solar wind dynamic pressure can compress the magnetosphere, increasing magnetic pressure (and consequently magnetic field strength) in the lobes (Fairfield & Jones, 1996; Milan et al., 2004; Nakai et al., 1991; Slavin et al., 1985; Sun et al., 2020).

Observations from the Mercury Surface, Space Environment, Geochemistry and Ranging (MESSENGER) mission have revealed that the low plasma β environment at Mercury's orbit enhances dayside magnetic reconnection rates, and the small size of Mercury's magnetosphere results in a Dungey cycle timescale of only a few minutes (DiBraccio et al., 2013; Siscoe et al., 1975; Slavin et al., 2009, 2010, 2019). Imber and Slavin (2017) identified periods in which the lobe magnetic flux is enhanced before quickly diminishing to its background state, characterizing the loading and unloading cycle of the magnetotail lobe of Mercury with a median timescale of 3.25 min. Modeling efforts made by Aizawa et al. (2021), Exner et al. (2018, 2020), Fatemi et al. (2020), Lavorenti et al. (2022), Li et al. (2023), and Trávníček et al. (2010) have demonstrated Mercury's global response to changes in dayside magnetic reconnection rates, in which enhanced dayside reconnection rapidly changes magnetic topology, increases the strength of the lobes, and increases magnetopause flaring. Chen et al. (2023) also found that dayside magnetic reconnection erodes magnetic flux from the dayside, lowering the altitude of the dayside magnetopause boundary as measured by MESSENGER. Furthermore, the magnetosphere of Mercury is highly compressible due to the strong solar wind forcing in the inner heliosphere (Exner et al., 2018; Fatemi et al., 2020; Jia et al., 2019; Korth et al., 2017; Slavin et al., 2014, 2019; Winslow et al., 2020; Zhong et al., 2015). Enhanced solar wind dynamic pressure compresses the magnetosphere, inducing currents that flow across the conductive core at Mercury (Johnson et al., 2016; Slavin et al., 2014), and increasing magnetic field strength in the lobes (Slavin et al., 2010, 2012; Sun et al., 2020). The strength of the magnetotail lobe field is thus an important metric to track the cycle of flux addition and removal through reconnection, explore the influence on upstream dynamic pressure, and to provide insights into global magnetospheric dynamics at this fascinating planet.

Studies at Earth (Fairfield & Jones, 1996), Jupiter (Kivelson & Khurana, 2002), and Saturn (Jackman & Arridge, 2011), have applied criteria to identify times when orbiting spacecraft were sampling the magnetotail lobes, and in turn calculated the average fall-off of the lobe field strength with increasing radial distance from the planet. At Mercury, Slavin et al. (2012) utilized lobe field observations from a total of four spacecraft flybys (three from MESSENGER, one from Mariner10) to estimate the fall-off of lobe magnetic field strength with radial distance. This initial study concluded that the lobe field strength varied greatly over the four flybys, and likely depends on rates of magnetopause reconnection on the dayside. However, these conclusions were tentative because they were only based on the magnetic field of the four lobe field observations at Mercury available at the time. A more robust analysis of the many lobe field observations throughout MESSENGER's orbital phase is required to more precisely characterize the nominal lobe field fall-off and understand how lobe field intensity depends on upstream conditions at Mercury.

In this study, we utilize MESSENGER observations to analyze the properties of Mercury's magnetotail lobe, with an aim to first quantify the nominal lobe field conditions and then to explore periods when the magnetic flux stored in the lobes is either enhanced or diminished compared to this nominal state. In Section 2, we introduce the MESSENGER mission and its relevant instrumentation before detailing criteria used to identify the lobe. Section 3 presents results of this lobe field classification, including the spatial distribution of MESSENGER lobe detections (Section 3.1) and the expression for the fall-off of magnetic field strength with radial downtail distance (Section 3.2). We then demonstrate the variability of lobe field detections through an analysis of four lobe field observations made along consecutive MESSENGER orbits (Section 3.3) before linking this variability in lobe field strength to upstream solar wind conditions across our entire data set (Section 3.4). Section 4 contextualizes our results within the lobe field fall-off expressions of Earth, Jupiter, and Saturn, and Section 5 concludes with a brief summary. This work also establishes context for the upcoming BepiColombo mission by outlining both the nominal and the extreme behavior which can be observed in Mercury's lobes. BepiColombo's two spacecraft will provide simultaneous measurements of Mercury's dayside and magnetotail environment, yielding an optimal

opportunity to further explore the relationship between the solar wind and the lobe magnetic field (Benkhoff et al., 2021; Milillo et al., 2020).

2. Methodology

2.1. Instrumentation

MESSENGER began its orbit around Mercury on 18 March 2011 with a 12 hr orbital period. The spacecraft was in a polar orbit with periapsis near the north magnetic pole at ~1.1 Mercury radii ($R_M = 2{,}440$ km) and apoapsis out in the solar wind at ~7.3 R_M. On 16 April 2012, MESSENGER's apoapsis decreased to ~5.5 R_M and its orbital period shrank to ~8 hr, increasing the total time spent within the magnetosphere while still sampling the solar wind along every orbit. MESSENGER was deliberately crashed into the surface of Mercury of 30 April 2015. The spacecraft sampled throughout the Mercury plasma environment during its more than 4 years orbital lifetime, measuring the solar wind, magnetosheath, and magnetosphere of Mercury along each of its more than 4,000 orbits.

In this study, we analyze the Mercury plasma environment through in situ measurements obtained by the magnetometer (MAG) (Anderson et al., 2007) and Fast Imaging Plasma Spectrometer (FIPS) (Andrews et al., 2007) instruments onboard MESSENGER throughout its orbital lifetime. The MAG instrument measured the three component magnetic field at a maximum 20 Hz sampling rate (Anderson et al., 2007). Our study utilizes all ~4 years of MESSENGER data, so we downsample MAG measurements to 1 Hz resolution. We report magnetic field measurements in the solar wind-aberrated Mercury solar magnetospheric (MSM') coordinate system, which is centered on the magnetic dipole. This coordinate system is offset from the center of the planet because the center of the dipole field of Mercury is positioned ~0.2 R_M northward of its spin axis (Anderson et al., 2011; Johnson et al., 2012). The MSM' coordinate system also accounts for aberration effects due to the orbital velocity of Mercury. The aberration angle was averaged daily and varies from 5.6° to 8.4° throughout a Mercury orbit. $X_{MSM'}$ points toward the Sun, $Z_{MSM'}$ points toward the north magnetic pole, and $Y_{MSM'}$ completes the right-hand coordinate system.

FIPS measured the energy per unit charge (E/q), time of flight, and angle of incidence for ions within an energy range 0.05–13 keV taken over 64 energy bins. While the instantaneous field of view (FOV) of FIPS was 1.4π sr, MESSENGER's sunshade partially blocked incoming plasma into the detector, resulting in an effective FOV of ~1.15π sr. FIPS measurements are therefore limited to plasma traveling transverse to the Mercury-Sun line, which excludes anisotropic plasma flows that move radially outward from the Sun (Gershman et al., 2013; Raines et al., 2011). This FOV effect is less relevant for isotropic plasma populations. The details of how our study handles the FIPS FOV constraint is written in Section 2.2.

2.2. Lobe Field Classification

MESSENGER's orbit was highly elliptical, with a periapsis consistently near the northern geographic pole of Mercury. As a result, the spacecraft spent far more time within the southern lobe of Mercury's magnetotail compared to that of the northern lobe throughout its lifetime. Our study is interested in the properties of the magnetotail lobe field downstream of the planet (~1.5–5.0 R_M), and therefore our analysis is limited to the southern magnetotail lobe where MESSENGER has provided sufficient downstream data coverage. To identify MESSENGER observations of the lobe, we define a set of empirically determined criteria that are based on both the location of the spacecraft and the in-situ data obtained via the MAG and FIPS instruments. These criteria were selected based on known properties of the lobe magnetic field at Mercury. We establish a set of conditions that seek to represent our understanding of the lobe field characteristics as quantifiable measures. The following conditions are evaluated for each orbit, and an example is presented in Figure 1.

1. The southern magnetotail lobe is located within the magnetosphere on the nightside of the planet. Therefore, we select times along each orbit in which MESSENGER sampled between the nightside magnetopause and the terminator plane ($X_{MSM'} = 0$). To identify the magnetopause crossing, we refer to the list of magnetopause and bowshock boundary crossings throughout the MESSENGER mission provided by Sun (2023). This boundary crossing list was generated by visually identifying boundary crossings based on rotations and amplitude changes in the MAG data throughout the MESSENGER mission and has been updated since its publication in Sun et al. (2020). The updated version will be referred to as SBC2023 throughout the remainder of this paper. An example of an orbital segment analyzed for lobe field signatures is shown in Figures 1f and 1g.

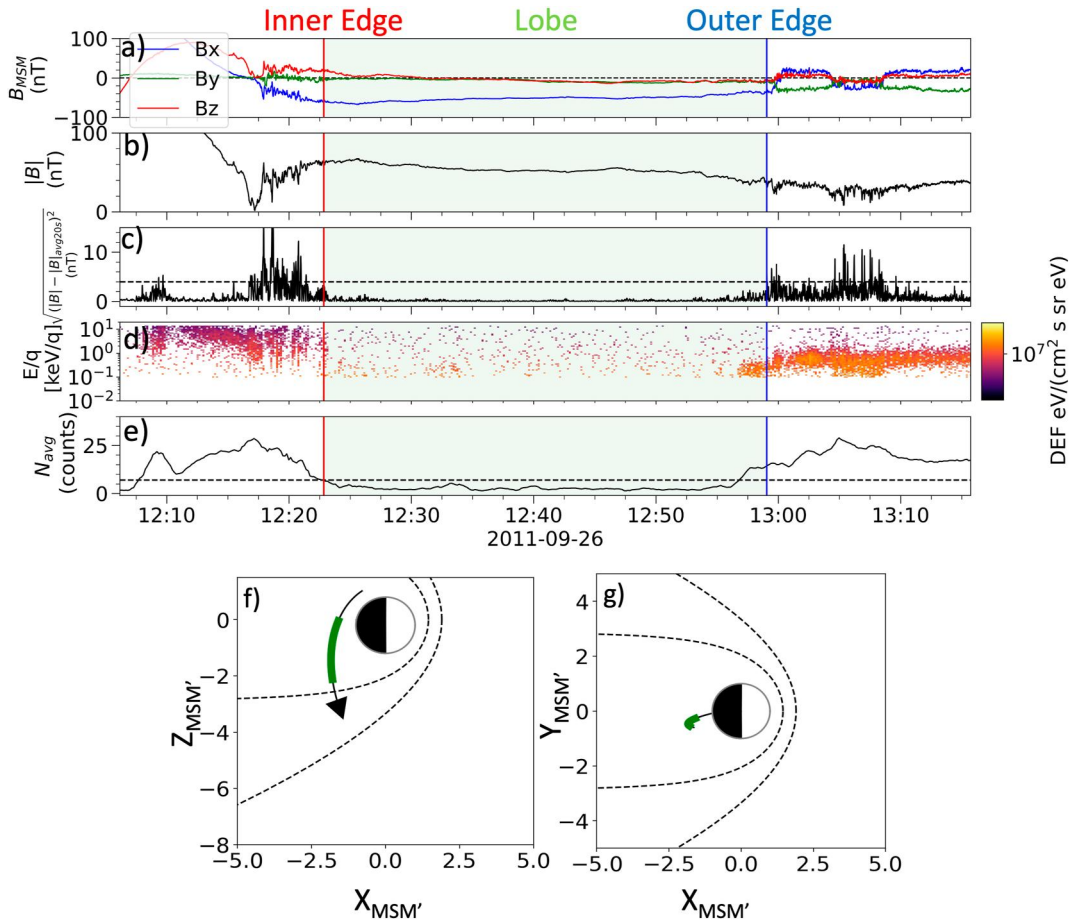


Figure 1. Mercury Surface, Space Environment, Geochemistry and Ranging tail lobe detection on 26 September 2011. (a) Three-component magnetic field in *MSM′* coordinate system. (b) Magnetic field magnitude, (c) $\sqrt{\left(|B| - |B|_{20savg}\right)^2}$, with dashed line representing cutoff for magnetosheath/plasma mantle determination. (d) Differential energy flux (DEF) spectrogram determined by Fast Imaging Plasma Spectrometer (FIPS). (e) Average number of bins with a registered count in the FIPS data averaged over 25 samples (5 min), dashed line represents cutoff for plasma sheet determination. Red/blue lines represent inner and outer edges of the lobes, with the shaded green representing the extent of the magnetotail lobe. (f, g) Show the portion of MESSENGER's orbital trajectory plotted in the time series above in the XZ/XY_{MSM} planes, with the green line representing the magnetotail lobe portion of the orbit. The outer and inner dashed black lines represent the nominal bowshock and magnetopause distances determined by Shue et al. (1997) and Winslow et al. (2013).

2. The open magnetic field lines that comprise the southern magnetotail lobe must point anti-sunward as they emanate from the southern pole of Mercury and are dragged downstream with the flowing solar wind (Korth et al., 2015; Rong et al., 2018; Slavin et al., 2010). We therefore require $B_{\mathrm{X,MSM'}} < 0$ for a measurement to classify as lobe field. Furthermore, the magnetic field within the lobe is characterized by a steady (low variability) magnetic field magnitude (|*B*|) compared to the high variability of |*B*| found in the magnetosheath (Imber & Slavin, 2017; Jasinski et al., 2017). To quantify this variability, we define a parameter $\sqrt{\left(|B| - |B_{avg20}|\right)^2}$, in which $|B_{avg20}|$ is the 20 s (20 measurement) point running average of magnetic field magnitude (Figure 1c). We require $\sqrt{\left(|B| - |B_{avg20}|\right)^2}$ to not exceed 4.0 nT for 3 min on either side of a measurement for all measurements within that window to be considered lobe field. These values were empirically determined to best fit the visual distinction between the steady |*B*| found in the lobe and highly variable |*B*| within the magnetosheath or the boundary region characterized by magnetosheath plasma into the magnetosphere known as the plasma mantle (DiBraccio et al., 2015; Jasinski et al., 2017).

3. The plasma density contained within the magnetotail lobe is lower than that found within the plasma sheet (Poh et al., 2017b, 2018; Sun et al., 2017). We utilize FIPS measurements of differential energy flux (Figure 1d) to identify the boundary between the lobe field and the plasma sheet. The number of energy bins (N) that contain counts was derived from the Derived Data Records of processed FIPS data downloaded from NASA's Planetary Data System. We then take a point running average of N over five FIPS scans (~1 min) to generate N_{avg} (Figure 1e). A threshold boundary of 7 counts for N_{avg} was empirically determined to separate the plasma sheet from the magnetotail lobe. N_{avg} must remain below this threshold 5 min on either side of a measurement for all measurements within that window to be considered lobe magnetic field.

The lobe field is defined when all of these conditions are simultaneously met within an orbit. The "inner" and "outer" edge of the lobe are defined with reference to the Sun-Mercury axis ($X_{MSM'} = 0$), where inner edge refers to the edge of the lobe closer to this axis, and the outer edge refers to edge of the lobe further from this axis. We define the outer edge of the lobe as the outermost point within the 3 min window in which $\sqrt{\left(|B| - |B_{avg20}|\right)^2}$ remained below 4.0 nT. Similarly, we define the inner edge of the lobe as the innermost point within the 5 min window in which N_{avg} remained below 7 counts. The green section in Figure 1 highlights the lobe field extent for an orbital segment that begins at 11:50 on 26 September 2011. MESSENGER's trajectory begins in the northern hemisphere near periapsis and traverses the plasma sheet moving southward at ~12:15. N_{avg} decreases below the threshold of 7 counts at 12:22:50, defining the inner edge of the lobe field. MESSENGER remains in the lobe for more than 30 min before the magnetic field variability $\left(\sqrt{\left(|B| - |B_{avg20}|\right)^2}\right)$ parameter increases above the threshold of 4.0 nT at 12:59:03, defining the outer edge of the magnetotail lobe. Due to MESSENGER's orbital geometry and Mercury's orbit around the Sun, roughly half of MESSENGER's traversals of the magnetotail are "descending" in which MESSENGER moves from the northern hemisphere near periapsis to the nightside magnetosphere in the southern hemisphere, as is the case for the example in Figure 1. For an "ascending" orbit (MESSENGER moves from the southern hemisphere on the nightside toward periapsis in the north), the chronology of these features is reversed: MESSENGER enters the magnetosphere from the magnetosheath/plasma mantle on the nightside before traversing the lobe and entering into the plasma sheet.

We note that while we used the FIPS condition to identify the inner edge of the lobe and the MAG variability condition to identify the outer edge of the lobe, applying the same criteria to the opposite edge of the lobe often yields similar results for the definition of the lobe field boundaries. For example, as we can see in Figure 1, $\sqrt{\left(|B|^2 - |B_{avg20}|\right)^2}$ exceeds 4.0 near the inner edge of the lobe identified by FIPS. This is because the magnetic field in the plasma sheet is often highly variable due to its low magnitude and large surrounding plasma density. Similarly, N_{avg} exceeds 7 counts near the outer edge of the lobe identified by MAG because the magnetosheath contains higher density shocked solar wind plasma compared to the low plasma density in the lobe. However, as mentioned in Section 2.1, the FIPS instrument is partially blocked by the Sun shade, limiting the FOV of the instrument particularly with respect to plasma moving toward and away from the Sun. The distribution of plasma within the plasma sheet is more isotropic than the largely anti-sunward flows of the magnetosheath/plasma mantle (Raines et al., 2011). The impact on FOV is therefore small within the plasma sheet, but greatly influences measurements of the magnetosheath/plasma mantle. As a result, we use FIPS data to identify the inner edge of the lobe associated with the plasma sheet and MAG data to identify the outer edge of the lobe associated with the magnetosheath/plasma mantle.

3. Results

3.1. Spatial Distribution

We apply the lobe classification scheme on a total of 4,075 MESSENGER orbits from 23 March 2011 to 29 April 2015. Of those 4,075 orbits, 455 were positioned mostly within the YZ plane and did not cross the magnetopause on the nightside in the southern ($-Z_{MSM'}$) MSM' magnetosphere. We therefore exclude those orbits due to unfavorable orbital geometry. We then define the orbital segments of the remaining 3,620 orbits via the process described in Section 2.1. Two hundred and eighty-eight of those 3,620 orbital segments did not possess sufficient FIPS data to perform the lobe classification analysis, leaving us with 3,332 orbital segments. Of those 3,332 segments, 1,258 contain intervals of data that pass the lobe classification analysis. We note that for 16 of those 1,258 orbital segments, the classification mistakenly identified a northern magnetic pole pass of Mercury as lobe

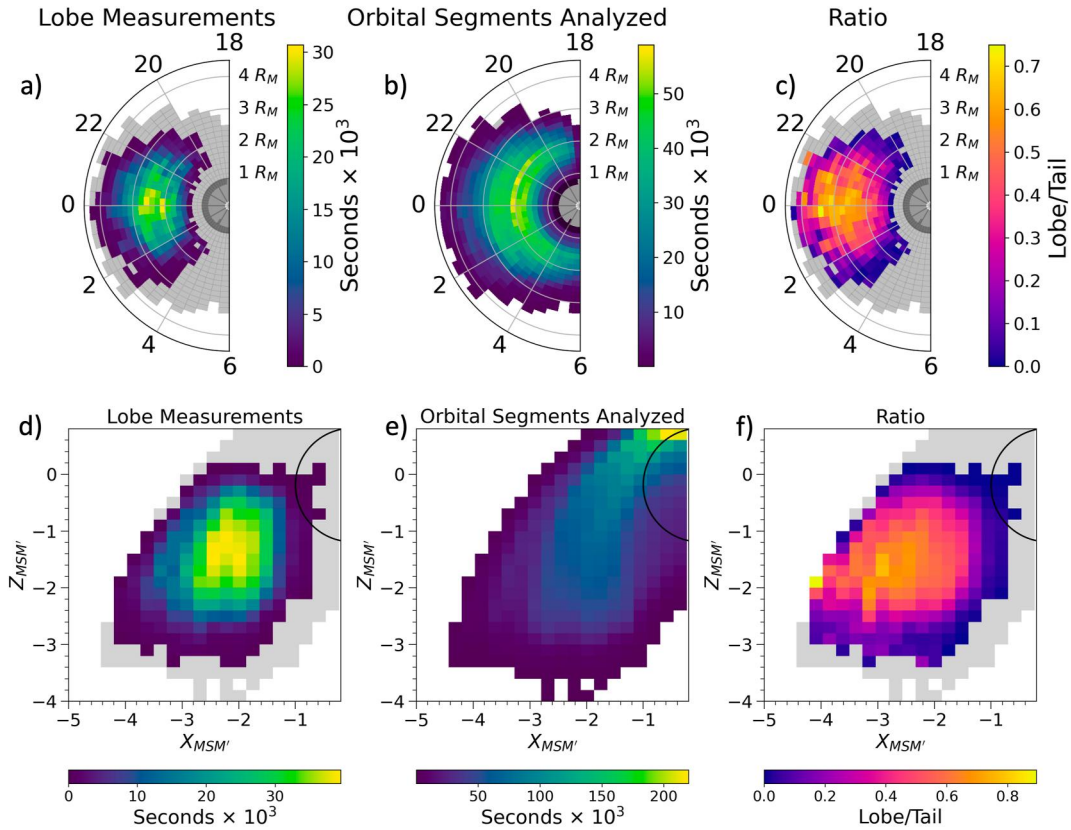


Figure 2. Spatial distribution of Mercury Surface, Space Environment, Geochemistry and Ranging (MESSENGER) lobe magnetic field measurements projected into polar coordinates (a–c) and onto the $XZ_{MSM'}$ plane (d–f). The bin size for the polar plots are 0.17 R_M in the radial direction and 6° in the theta direction. The bin size for the $XZ_{MSM'}$ plane is 0.17 $R_M \times 0.17$ R_M. The numbers along the perimeter of the polar plots represent local time. Panels (a) and (d) are colored by the total seconds in which MESSENGER encountered lobe magnetic field. Panels (b) and (e) are colored by the time MESSENGER spent in each spatial in which the lobe classification was applied. Panels (c) and (d) are colored by the ratio of the two, representing the frequency of lobe field detections in each spatial bin. In all plots, gray bins indicate 0 lobe field detections despite MESSENGER sampling that region, and white represents regions in which MESSENGER did not sample.

field. These clear mis-identifications were removed, resulting in 1,242 lobe field detections out of 3,332 MESSENGER orbits (37%). The mean duration of the lobe field encounter along an orbit was 33 min, ranging from ∼2–90 min. The relatively low detection frequency of 37% is a lower limit and is the result of a combination of orbital sampling effects and the conservative empirical conditions we applied in detecting the lobe. This is discussed further in the following two paragraphs.

Figure 2 shows the spatial distribution of the lobe fields detected by MESSENGER with respect to total orbital coverage considered for this analysis. The magnetotail lobe is detected most frequently in the local time (LT) hours around midnight and is detected less frequently toward the dawn and dusk terminators of Mercury (Figure 2c). This trend is particularly clear on the dawnside where we see almost no evidence for lobe magnetic field signatures between 4 and 6 hr LT (Figure 2a) despite sufficient MESSENGER coverage (Figure 2b). This LT preference helps explain the relatively low percentage of orbits in which lobe fields are detected (37%); orbits that sample primarily dawn/dusk LT on the nightside have an unfavorable orbital geometry to detect lobe fields that are found most frequently around midnight LT.

Southern lobe field detections are most frequent when $-2\ R_M < Z_{MSM'} < -1\ R_M$ at $X_{MSM'} \sim -3\ R_M$ downtail (Figure 2f). The peak ratio between time spent in the lobe and total time spent within that spatial bin is >0.73, suggesting there are regions of the magnetosphere that are consistent with lobe magnetic field properties more than 73% of the time. Therefore, even in the highest detection frequency bins, there are still many orbits (∼27%) in which lobe magnetic fields are not detected despite favorable orbital geometry. In these cases, a lack of a lobe

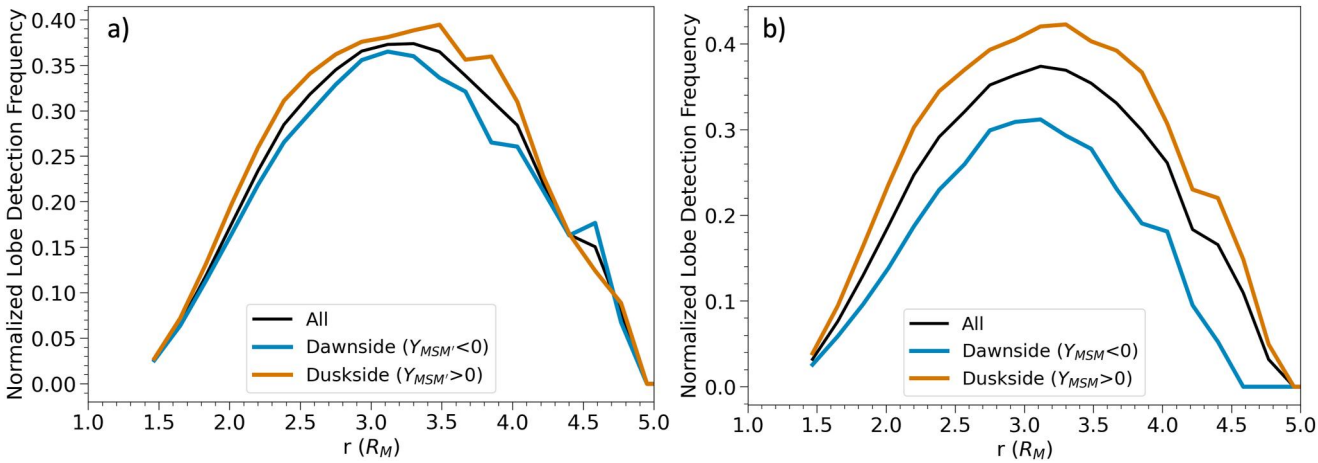


Figure 3. Detection frequency of lobe fields in 0.17 R_M radial spatial bins. Left-hand panel (panel a) shows the lobe field detection frequency in the aberrated reference frame (*MSM′*), and right-hand panel (panel b) shows the lobe field detection frequency in the non-aberrated reference frame (*MSM*). Black line represents the detection frequency for all of the lobe magnetic field data, brown represents detection frequency on the duskside ($Y_{MSM'}/Y_{MSM} > 0$) and turquoise represents detection frequency on the dawnside ($Y_{MSM'}/Y_{MSM} < 0$).

field detection is the result of a highly fluctuating magnetotail lobe field and/or FIPS detections of plasma within the magnetotail lobe indicative of an extended plasma mantle or extended current sheet. Either of these possibilities would exclude observations from our lobe field data set based on the empirically determined criteria for lobe field detections discussed in Section 2.2. We note that we intentionally set these criteria to be quite conservative because our further analysis of the lobe field requires all measurements to be unequivocally within the magnetotail lobe, which has likely resulted in some MESSENGER observations of the lobe field to be omitted from the data set. Thus, the reported orbital lobe field detection frequency of 37% is a lower limit.

Next, we wish to examine the rate of lobe field detections with radial distance downtail. To do this, we split the data into 0.17 radial bins in the spherical coordinate system ($r = \sqrt{X^2_{MSM'} + Y^2_{MSM'} + Z^2_{MSM'}}$) and plot the average value of the detection frequency in each bin (Figure 3). We see a peak in the average lobe detection frequency at $r \sim 3.2\ R_M$ (Figure 3). When we divide lobe field detections based on LT, we find that the lobe field is detected slightly more frequently on the duskside ($Y_{MSM'} > 0$) than on the dawnside ($Y_{MSM'} < 0$). This asymmetry is reported in the aberrated coordinate system (*MSM′*), and is therefore not due to aberration effects (Figure 3a). Poh et al. (2017a) showed that Mercury's plasma sheet is thicker on the dawnside than on the duskside in the aberrated (*MSM′*) reference frame, which would decrease total time spent in the dawnside lobe compared to the duskside. Our lobe classification methodology identified 357 hr of lobe fields on the duskside of Mercury and 327 hr on the dawnside in the aberrated reference frame (*MSM′*). In a study by Korth et al. (2014), the spatial distribution of proton flux and pressure at Mercury was assessed using FIPS observations, revealing that these properties are significantly higher on the dawnside than the duskside in the non-aberrated reference frame. This result is consistent with magnetohydrodynamic with embedded particle-in-cell simulations of Mercury's magnetotail described Chen et al. (2019) which also found enhanced proton density on the dawnside of Mercury compared to the duskside, also in the non-aberrated frame. In the non-aberrated (*MSM*) reference frame, we report much higher lobe field detections on the duskside than the dawnside (Figure 3b), with 447 hr detected on the duskside ($Y_{MSM'} > 0$) and 237 hr detected on the dawnside ($Y_{MSM'} < 0$). Consequently, the enhanced proton density on the dawnside would lead to higher *N* values, and therefore fewer lobe field detections in that region as opposed to the duskside in the non-aberrated reference frame.

In addition to examining the lobe field locations, we explore the internal distribution of magnetic field strength within the lobe fields at Mercury. The spatial distribution of the lobe magnetic field orientation and strength is shown in the *MSM′* coordinate system in Figure 4. These lobe field maps provide some interesting insights into the nominal structure of the lobe magnetic field. For example, we observe a symmetrical distribution of the *BY* component of the lobes, in which B_Y points predominately in the $-Y_{MSM'}$ on the duskside and predominately in $+Y_{MSM'}$ direction on the dawnside (Figure 4c). This symmetry in *BY* is present in the aberrated coordinate system,

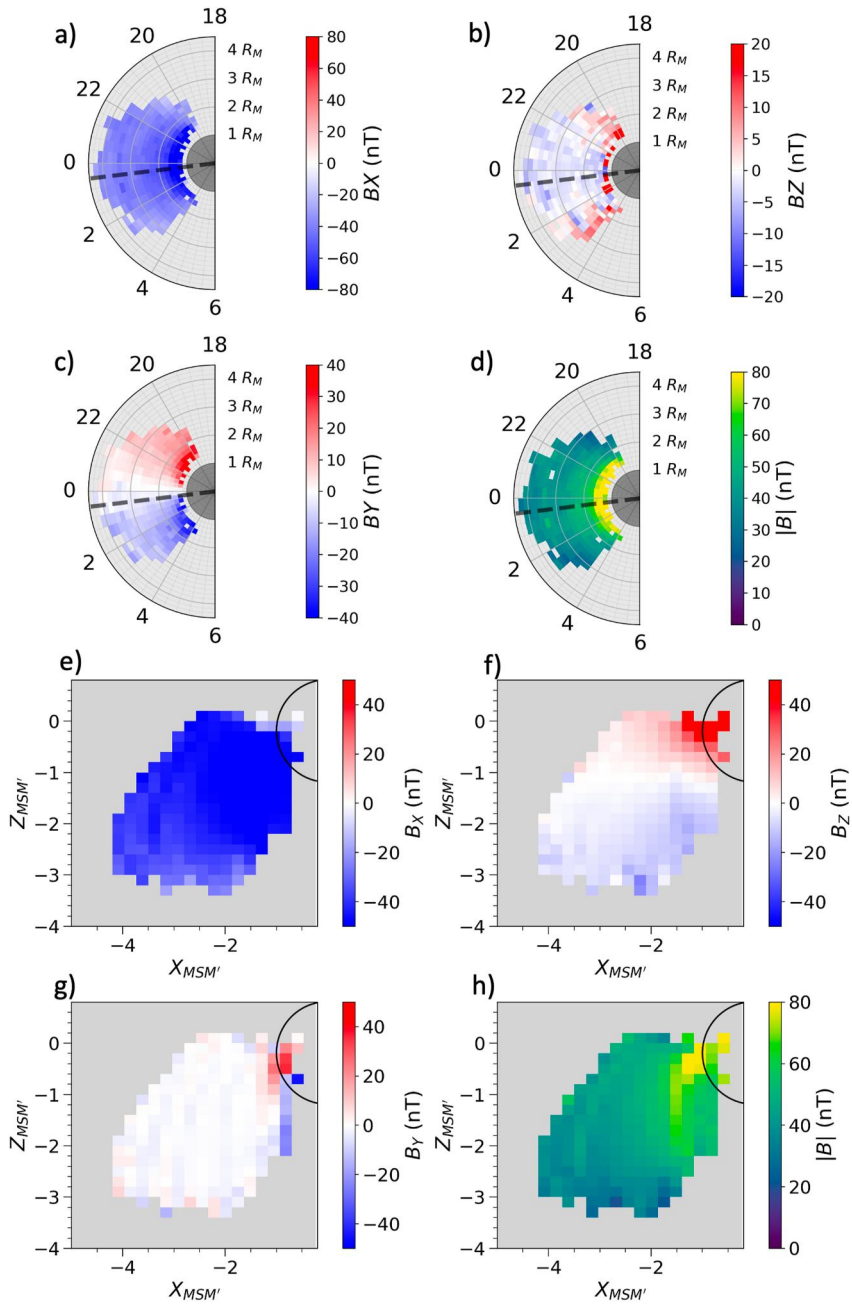


Figure 4. Spatial distribution of lobe field crossings in the same format as Figure 2. Spatial distribution of lobe field is colored by B_X (a, e), B_Y (c, g), B_Z (b, f), and $|B|$ (d, h). X, Y, and Z are in the aberrated MSM' coordinate system. Gray bins represent spatial bins with no lobe field detections. In the polar projections, the black dashed line is positioned at the average aberration angle (7°) during lobe field observations.

suggesting the lobe fields align in the direction of the solar wind flow in Mercury's orbital, aberrated reference frame in agreement with numerical models, rather than directly aligning with the average Mercury/Sun line, represented as a black-dashed line in Figure 4.

Our analysis is limited to 4.7 R_M downtail and is exclusive to the southern lobe due to MESSENGER's orbital geometry. Mio, one of the two spacecraft of BepiColombo, will sample further downtail (~5.8 R_M), as well as more evenly sample the northern and southern lobes (Milillo et al., 2020). If the asymmetry in the $Y_{MSM'}$ component of the lobe is correlated with upstream $B_{\mathrm{Y,MSM'}}$ in the IMF as posited above and in agreement with

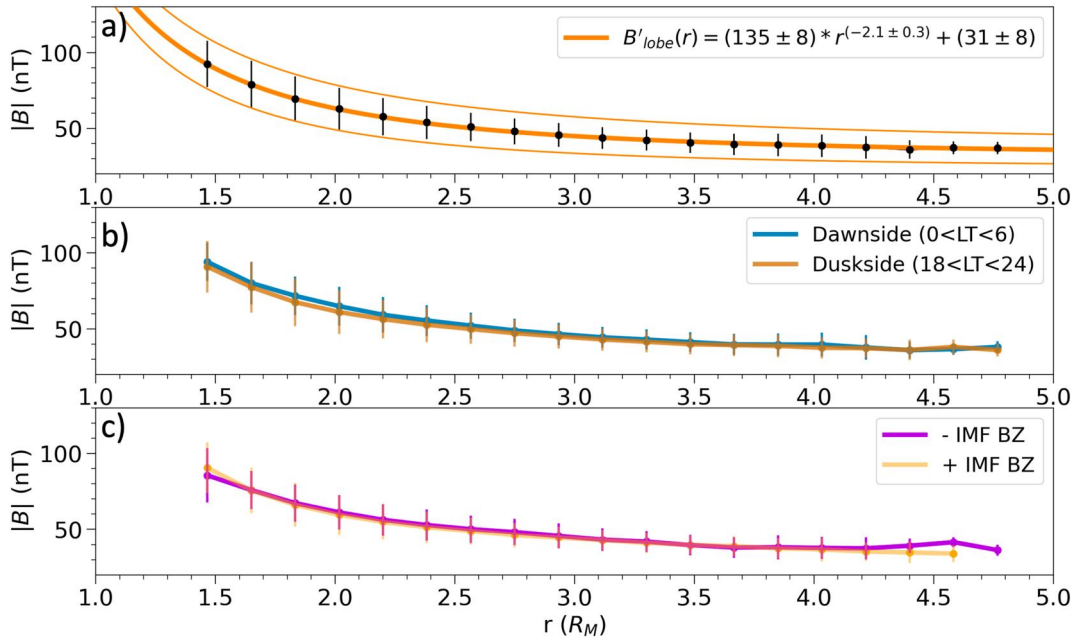


Figure 5. Lobe magnetic field strength versus radial distance from Mercury. Each point represents average magnetic field strength within each 0.17 R_M radial bin. The error bars represent 1 standard deviation (σ) within each bin. (a) Center orange curve represents the curve best fit expressed in the function to the upper right. Upper and lower orange lines represent the upper and lower bounds of the uncertainty in the best fit curve. (b) Lobe fall-off for exclusively duskside (18 < local time [LT] < 24, brown) and dawnside (0 < LT < 6, turquoise) lobe field encounters. (c) Lobe fall-off for exclusively lobe field measurements observed under negative interplanetary magnetic field (IMF) *BZ* conditions (purple) and positive IMF *BZ* conditions (gold).

numerical models, then we would expect the opposite asymmetry to occur in the northern lobe. In this scenario, the $+B_Y$ component of the IMF would yield an enhancement of the lobe $+Y_{MSM'}$ component on the duskside of the northern lobe, just as it may have on the dawnside of the southern lobe. Future studies using orbital data collected by BepiColombo will enhance our understanding of the nominal lobe field spatial distribution and orientation at Mercury.

3.2. Lobe Field Fall-Off

The lobe field strength is generally strongest near the planet and becomes gradually weaker with radial distance (Figures 4d and 4h). The extent to which the lobe magnetic field falls off with radial distance is important for understanding pressure balance within the system. An increase in solar wind dynamic pressure creates a pressure imbalance in the system and exerts a force on the flared magnetopause, leading to its compression (Fairfield & Jones, 1996; Nakai et al., 1991). After compression, the solar wind dynamic and thermal pressure is again completely balanced by the magnetic pressure supplied by the lobe magnetic field. Furthermore, an expression for the typical lobe field fall-off with radial distance will help us determine typical versus atypical lobe field encounters throughout our data set. We fit the points to a curve of the functional form: $B'_{lobe} = Cr^{-\alpha} + b$, where r is the radial distance from Mercury and D, α, and b are the free parameters of the fit. This functional form is the same used for the lobe field at the Earth (Fairfield & Jones, 1996), as well as Jupiter (Kivelson & Khurana, 2002) and Saturn (Jackman & Arridge, 2011). Figure 5 plots the average magnetic field amplitude measurements in the lobe (B_{lobe}) within the same radial spatial bins used in Figure 3. Then, we apply a least square fit to the above function weighted by the standard deviation (σ) of each point to estimate the offset coefficient b. Then, we subtract this estimate from the average lobe data within each bin to obtain $(B'_{lobe} - b) = Cr^{-\alpha}$. Next, we linearize the function by taking the $\log_{10}$ of each side. We then perform a linear fit in this log-log space, weighting each point in the standard methodology outlined in Bevington and Robinson (2003), and detailed in the case for a lobe magnetic field in Jackman and Arridge (2011). The resulting expression for the nominal magnetotail lobe field fall-off with radial distance r in R_M is:

$$B'_{lobe}(r) = (135 \pm 8) * r^{(-2.1 \pm 0.3)} + (31 \pm 8) \quad [nT] \quad (1)$$

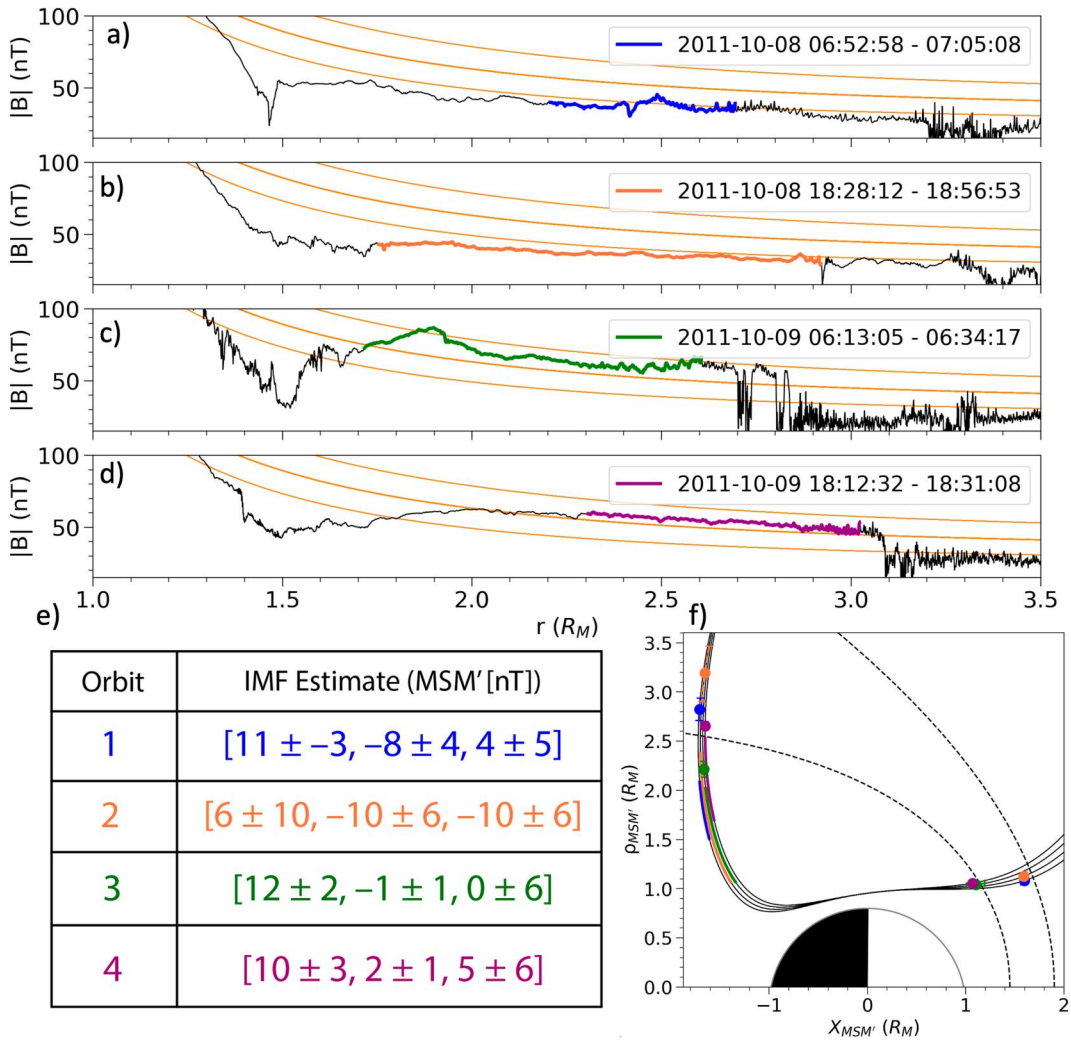
Lobe field classifications were made out to ~4.7 R_M, where MESSENGER's coverage ended within the magnetosphere (Figure 5a). The α value of -2.1 ± 0.3 is larger (less negative) than the magnetic field fall-off for a pure dipole field ($\alpha = -3$), indicating the magnetic field is stretched downtail from the dipole field configuration. Using lobe field observations from four spacecraft flybys of Mercury, Slavin et al. (2012) estimated α individually for each flyby. Their estimated values of α ranged from -5.4 to -1.6, defining a range within which our more precise estimate falls. We note that the lobe field strength relationship is not significantly different if we plot the duskside and dawnside separately (Figure 5b).

The range of α values, derived from the fall-off expression of the lobe field estimated through Mariner 10 and MESSENGER flybys as discussed in Slavin et al. (2012), was hypothesized to be attributed to varying rates of dayside reconnection during these passages through Mercury's magnetosphere. The lowest value of α (corresponding to the fastest fall-off with distance) occurred during northward IMF conditions (low rates of dayside reconnection), while the highest value of α occurred during southward IMF conditions (high rates of dayside reconnection). Slavin et al. (2012) suggested that this was due to increased magnetopause flaring under enhanced dayside reconnection, leading to more lobe flux further downstream from Mercury. To explore the relationship between dayside reconnection and lobe field strength for our data set of lobe field traversals, we estimate the upstream IMF orientation for each lobe crossing by averaging the inbound and outbound IMF estimates for the same orbit in which the lobe field was detected. Using the list of bowshock crossings compiled in SBC2023, we take a 10 min average of the magnetic field upstream of each bowshock crossing and then average the two together to get an individual IMF estimate for each orbit in our data set. This method leads to an IMF estimation with limited accuracy due to the temporal separation between lobe field and IMF measurements. While it is possible that the IMF has remained steady between the IMF measurement and lobe field detection, it is also likely that the IMF has shifted significantly between these two observations (He et al., 2017; James et al., 2017). To limit the effect of shifting IMF orientation, we omit lobe field detections in which the uncertainty in the $Z_{MSM'}$ component of the estimated IMF is greater than 7 nT, leaving us with 679 orbits in which MESSENGER sampled the lobe and the IMF was stable on either side of the bowshock.

When we compare the lobe field strength relationship with r under positive/negative IMF BZ conditions, we see that the lobe field fall-off is not significantly different (Figure 5c). The values for α do not change significantly with IMF BZ as well, with $\alpha_+ = -2.0 \pm 0.5$ for positive IMF BZ conditions, and $\alpha_- = -2.3 \pm 0.2$ for negative IMF BZ conditions. We note that this conclusion does not entail that IMF BZ has no impact on lobe field strength. Theory and modeling efforts have shown lobe field strength increases as dayside magnetic reconnection is enhanced under negative IMF BZ conditions (Fatemi et al., 2020; Lavorenti et al., 2022). These modeling efforts are quasi-static solutions of Mercury's magnetospheric response to upstream IMF conditions, and therefore cannot model the time scales in which the lobe flux is enhanced. However, MESSENGER observations of loading/unloading flux events suggest that, due to the fast Dungey cycle at Mercury, enhancements in lobe field strength likely last only 2–3 min before returning to the background lobe flux amount (Imber & Slavin, 2017). Therefore, our results suggest this momentary increase in flux is insufficient to result in a significant difference average lobe field strength across many orbits. This result is explored further in Section 3.4.

3.3. Four Orbit Case Study

We utilize the established average lobe field fall-off (Equation 1) as a reference point to evaluate the relative intensity of the lobe field measurements in our data set. Such a comparison is useful for assessing the surrounding magnetospheric conditions that contribute to variations in lobe magnetic field strength. For example, if the measured B_{lobe} at a certain r is stronger than predicted by Equation 1, then we may assume some physical process (e.g., enhanced magnetic flux entering the nightside due to reconnection or a compression of the magnetosphere due to an increase in solar wind dynamic pressure), has resulted in enhanced lobe field strength in the tail. To explore this further, we plot lobe magnetic field observations along four consecutive orbits from 8 to 9 October 2011 (Figure 6). Since each of these orbits samples a similar spatial regime, orbit-to-orbit variations observed in the lobe field strength are more likely to be attributed to changes in magnetospheric dynamics rather than being influenced by orbital sampling effects.



Orbit	IMF Estimate (MSM′ [nT])
1	[11 ± −3, −8 ± 4, 4 ± 5]
2	[6 ± 10, −10 ± 6, −10 ± 6]
3	[12 ± 2, −1 ± 1, 0 ± 6]
4	[10 ± 3, 2 ± 1, 5 ± 6]

Figure 6. Magnetic field strength (|*B*|) versus radial distance *r* along four consecutive orbits from 8 to 9 October 2011 (a–d), alongside the associated magnetopause crossing locations (e). The colored portion of the each plot indicates where our lobe classification scheme identified lobe magnetic field. The time marker in the upper right of each plot is the time at the start of the lobe field detection. The orange lines represent the lobe field fall off expression as shown in Figure 5. (e) A table of the interplanetary magnetic field (IMF) orientation during each lobe crossing, estimated from closest inbound/outbound IMF measurements. (f) Solid black lines represent MESSENGER's orbital trajectory for all four orbits analyzed, plotted in cylindrical coordinates. Outer/inner dashed curves represent the nominal location of the bowshock/magnetopause as described in Shue et al. (1997) and Winslow et al. (2013). The circles along the orbits represent the location of the 2 (dayside + nightside) magnetopause crossings as determined by SBC2023 along the orbit. The error bars on magnetopause crossing locations highlight the spatial range of magnetopause crossings determined in SBC2023. Solid lines along the orbit represent the portion of the orbit that was classified as lobe magnetic field. The color of the points and line segments correspond to the color of the associated magnetic field measurement plots (a–d).

The lobe field strength of these four orbits exhibit a significant orbit-to-orbit variability in comparison to the nominal lobe field estimated by Equation 1. Measurements of lobe strength along the first two orbits in this series (Figures 6a and 6b) generally fall below the nominal lobe field strength (B'_{lobe}) across values of *r*. On the other hand, lobe strength measurements along subsequent two orbits (Figures 6c and 6d) fall at or above B'_{lobe} estimates across *r*. This variability in lobe field strength within a very similar spatial region of the magnetosphere may be attributed to changes in dayside reconnection rates and/or solar wind dynamic pressure. Slavin et al. (2012) used lobe field measurements from four Mercury flybys to argue that upstream IMF orientation should impact the lobe magnetic field fall-off. They found large variability in lobe field strength from flyby to flyby. They posit this large timescale variability is due to different dayside magnetic reconnection conditions, with lobe field encounters

under northward IMF orientations exhibiting weaker strength and steeper fall-off compared to the flybys with associated southward IMF orientation. While reconnection at Mercury is thought to occur under a variety of upstream IMF orientations due to the low plasma β conditions in the inner heliosphere (DiBraccio et al., 2013), we expect magnetic reconnection on the dayside to be most efficient when the IMF points in the southward ($-Z_{MSM'}$) direction, which is anti-parallel to Mercury's dayside planetary magnetic field. Therefore, a change toward more southward IMF conditions at some time in between lobe field observations would enhance dayside magnetic reconnection rates and subsequently increase magnetotail lobe intensity as the open field lines populate the tail (Fatemi et al., 2020; Lavorenti et al., 2022). Furthermore, Jasinski et al. (2017) demonstrated plasma mantle observation frequency and proton density were higher for southward IMF conditions, which would also impact lobe field detections.

To explore the relationship between dayside reconnection and lobe field strength for these four orbits, we estimate the upstream IMF orientation for each lobe crossing by averaging the inbound and outbound IMF estimates for the same orbit in which the lobe field was detected. Using the list of bowshock crossings compiled in SBC2023, we take a 10 min average of the magnetic field upstream of each bowshock crossing and then average the two together to get an individual IMF estimate for each of the four orbits (Figure 6e). The uncertainty in magnetic field strength in each component of the estimated IMF is the standard deviation of the mean of the total 20 min of IMF measurements taken for our IMF estimate. This methodology is the same as that used in Romanelli et al. (2022) which compared the upstream IMF orientation to the average magnetotail orientation using MESSENGER observations. For these four orbits, it is difficult to assess the impact of IMF *BZ* on lobe field strength, as the uncertainty in IMF components is on the order of the estimated values. The orbit with the most ideal conditions for dayside reconnection (most southward IMF orientation) is the second orbit, which exhibited the weakest lobe field intensity, which is the opposite trend predicted from models of the magnetosphere under northward versus southward IMF conditions (Fatemi et al., 2020). We note that the measurements of IMF orientation occur up to 3 hr from the lobe field measurements, within which the IMF may have shifted orientation significantly. Indeed, James et al. (2017) concluded that the IMF at Mercury can shift orientation on the order of a few tens of minutes, suggesting the IMF may have changed significantly multiple times within the ∼3 hr between lobe field observations and solar wind observations. Exner et al. (2018) also showed under hybrid modeling conditions that Mercury's magnetosphere may shift radically in topology during IMF variations on the order of ∼10 min, highlighting the fast magnetospheric response time to IMF conditions.

The timescales of the magnetospheric response to enhanced dayside reconnection also play a role in the total lobe field intensity signature relative to the nominal field. A typical Dungey cycle at Mercury lasts roughly 2–3 min (DiBraccio et al., 2013; Slavin et al., 2010, 2021), so we expect the loading of magnetic flux in the lobe due to dayside reconnection to quickly unload as nightside reconnection commences (Imber & Slavin, 2017). On the third orbit (green), the lobe field enhanced at $r \approx 1.7\ R_M$ before returning to a baseline value, which then proceeded to fall-off consistently above the modeled lobe field fall-off. This small-scale enhancement lasted ∼3 min, consistent with a tail loading and unloading event discussed in Imber and Slavin (2017), and is likely the result of the rates of dayside and nightside magnetic reconnection. Also, for the first orbit (blue), we see a similar small-scale enhancement in lobe field at $r \approx 2.4\ R_M$ which lasts for ∼2 min before returning to a baseline value below the nominal lobe field fall-off, again consistent with a tail loading and unloading event. However, for the second orbit (orange), we see the lobe field is quite steady and remains consistently below the modeled lobe field fall-off from Equation 1 for 28 min, much longer timescales than a typical Dungey cycle. There is some evidence for a small enhancement in the lobe field during the second orbit at $r \approx 2.75\ R_M$ that lasted ∼1 min, but this feature is small compared to those observed along orbits 1 and 3. Furthermore, the lobe field for the fourth orbit (purple) lies consistently near the modeled lobe field fall-off for 19 min. These more steady lobe field detections vary in strength on the orbit-to-orbit timescale, but do not clearly exhibit the short timescale enhancements characteristic of the loading and unloading of magnetic flux often associated with dayside reconnection.

Next, we investigate the impact of magnetospheric compressions on the magnetotail lobe fields by highlighting the spatial extent of the lobe field detections along the orbital trajectories of each of the four orbits shown in Figures 6a–6d in cylindrical $\left(\rho_{MSM} = \sqrt{Y_{MSM'}^2 + Z_{MSM'}^2}\right)$ coordinates (Figure 6f). Along each of these four orbits, MESSENGER crossed the magnetopause boundaries twice: once on dayside of the planet and once on the nightside. We plot the location of the eight magnetopause crossings along these orbits as listed within SBC2023. The crossing of the magnetopause is often not clearly defined at a single location along a MESSENGER trajectory

and is therefore given as a range of locations in which the spacecraft may have crossed the magnetopause boundary multiple times. This range of crossings is shown as error bars in Figure 6f. Next, we compare the measured locations of the magnetopause crossing to the nominal magnetopause boundary determined by Winslow et al. (2013) to assess the compression or expansion of the magnetosphere. The dayside magnetopause crossings along the first two orbits (blue and orange) occur much further out than the nominal magnetopause boundary, whereas the magnetopause crossings from the subsequent two orbits (green and purple) lie along the nominal magnetopause boundary. On the nightside, the magnetopause crossings of the first two orbits again lie expanded outside the nominal magnetopause boundary. The nightside magnetopause crossing along the third orbit (green) lies well within the nominal boundary, and that of the fourth orbit (purple) lies along the nominal magnetopause boundary.

We would like to emphasize that the magnetopause boundary location, as determined by Winslow et al. (2013) and illustrated in Figure 6, was established based on MESSENGER observations spanning over 3 years (equivalent to approximately 12 Mercury years). Furthermore, Zhong et al. (2015) demonstrated that the average magnetopause boundary changes over the course of a Mercury year due to the eccentricity of Mercury's orbit. Specifically, the average magnetopause boundary is expanded near aphelion and contracted near perihelion. It is important to note that the Winslow et al. (2013) boundary calculation encompasses averages all magnetopause crossings at all heliocentric distances. During the four orbit case study shown above, Mercury is near aphelion (heliocentric distance $\approx$ 0.44 astronomical units [AU]). Consequently, we expect an expanded average magnetopause boundary during these four orbits compared to the nominal boundary described in Winslow et al. (2013). Our work focuses on the relative positions magnetopause boundaries rather than their absolute locations, which are influenced by heliocentric distance. Therefore, the magnetopause description provided by Winslow et al. (2013) serves as a useful reference point for comparing boundary locations to one another, despite representing an average location of a boundary that expands and contracts within a Mercury year.

This four orbit case study suggests an interesting correlation between lobe magnetic field strength and associated dayside/nightside magnetopause location. The first two orbits (blue and orange) have significantly lower lobe field strength measurements compared to $B'_{lobe}(r)$ (Equation 1) and the location of the dayside and nightside magnetopause crossings along these orbits implies the magnetosphere of Mercury is expanded compared to its nominal volume. On the other hand, the subsequent two orbits (green and purple) measured slightly enhanced lobe fields compared to $B'_{lobe}(r)$, and the associated location of the dayside and nightside magnetopause crossings implies a nominal or slightly compressed magnetosphere volume.

To further explore the relationship between measured lobe field strength ($B_{measured}$) and magnetopause location, we define a new value:

$$B_{scaled} = B_{measured}/B'_{lobe}(r) \tag{2}$$

B_{scaled} quantifies the relative magnitude of the lobe magnetic field compared to the expected lobe field strength at the given radial distance from Mercury. We compare the B_{scaled} values for the four lobe detections plotted in Figure 6 on the same figure to better visualize their relative strength across r (Figure 7a). B_{scaled} for the first two orbits (blue and orange) are consistently below 1, with an average of 0.71 $\pm$ 0.05 and 0.66 $\pm$ 0.03. These two average B_{scaled} values are in the bottom 4% of all 1,242 average B_{scaled} values in our study. On the other hand, the second two orbits (green and purple) fall above 1, with an average of 1.13 $\pm$ 0.06 and 1.08 $\pm$ 0.02. The uncertainties in these values is the standard deviation of the mean of B_{scaled} along each lobe crossing.

Figure 7b is a zoomed-in version of the nightside magnetopause crossings and nominal boundary location shown in Figure 6e. The distance to the curve defined by the magnetopause boundary expression as determined by Shue et al. (1997) and Winslow et al. (2013) is represented by d and is printed to the right of plot for each magnetopause location. A similar analysis was performed in Zhong et al. (2015) to measure the variability of the magnetospheric dimensions with heliocentric distance. We note that the sign of d depends on whether the measured magnetopause crossing falls within the nominal boundary ($d < 0$), or outside the nominal boundary ($d > 0$). For the first two orbits (blue and orange), $d = 0.17 \pm 0.09$ and 0.51 ± 0.26, indicating that the magnetosphere was expanded during these orbits. $d = -0.39 \pm 0.07$ for the third orbit (green), indicating the magnetosphere was compressed. The magnetopause crossing for the fourth orbit (purple) lies near the nominal position for the magnetopause boundary ($d = 0.02 \pm 0.04$). The uncertainty in d is a result of the magnetopause crossing extent as listed in SBC2023.

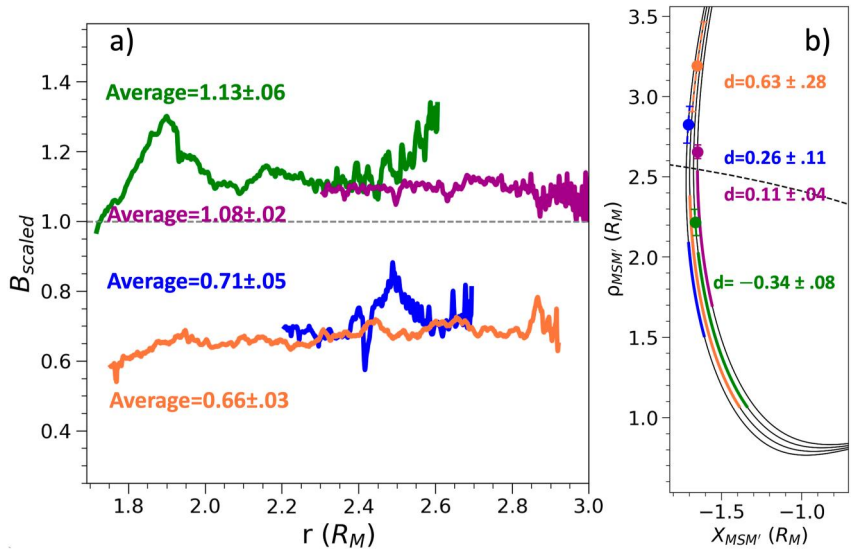


Figure 7. (a) B_{scaled} versus r for the same four lobe magnetic field measurements as shown in Figure 6. Gray dashed line indicates $B_{scaled} = 1$. Average value of B_{scaled} for each orbit is shown in the color of the associated lobe field, with the standard deviation of the mean shown as the uncertainty. (b) Zoomed-in version of Figure 6e with a focus on the nightside magnetopause crossings. The distance, d, to the nominal bowshock curve (dashed black line) as determined by Shue et al. (1997) and Winslow et al. (2013) is printed to the right and color-coded to the associated orbit. The uncertainty in d is a result of the magnetopause extent as listed in SBC2023.

3.4. B_{scaled} and External Conditions

We repeat the analysis from Section 3.3 for all 1,242 lobe magnetic field observations in our data set. To investigate the effects of dayside reconnection rates on B_{scaled}, we estimate the $Z_{MSM'}$ component of the IMF for each lobe magnetic field observation in our data set using the IMF estimation methodology described in Section 3.2, again omitting lobe field detections in which the uncertainty in the $Z_{MSM'}$ component of the estimated IMF is greater than 7 nT to limit effects of IMF variability. The Pearson correlation coefficient between B_{scaled} and the $Z_{MSM'}$ component of the estimated IMF is 0.59, suggesting no significant correlation between (Figure 8). This result is in contrast to Slavin et al. (2012), which attributed the flyby-to-flyby variability in lobe field strength to upstream IMF conditions during four spacecraft flybys of Mercury.

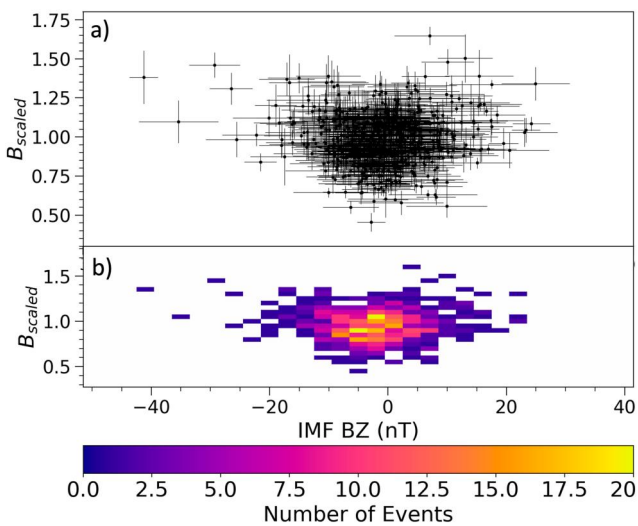


Figure 8. (a) Average B_{scaled} versus $Z_{MSM'}$ component of the estimated interplanetary magnetic field (IMF) orientation upstream of the Mercury bowshock. This plot only shows data for orbits in which the uncertainty in the $Z_{MSM'}$ component of the estimated IMF is <7 nT (679 orbits). Uncertainty in IMF $BZ_{MSM'}$ is the standard deviation of the mean throughout the upstream solar wind measurement. Uncertainty in B_{scaled} is the standard deviation of the mean throughout the lobe magnetic field extent. (b) Color map of panel (a) separated into a 30 × 30 mesh grid and colored by the number of events that fall within each bin. The uncertainty within each measurement is not considered when constructing the color map.

The lack of correlation between IMF $BZ_{MSM'}$ and B_{scaled} is likely due to the short timescales of the Mercury's magnetospheric response to dayside reconnection. The characteristic timescale (2–3 min) of the Dungey cycle at Mercury is much shorter that the timescales of a typical lobe field encounter (~30 min). Consequently, an enhancement of dayside reconnection due to IMF $BZ_{MSM'}$ conditions results in a short increase in lobe field intensity before a return to the background lobe field strength as nightside reconnection commences. The median timescale for the loading and unloading of magnetic flux in the lobe at Mercury is 3.25 min (Imber & Slavin, 2017). This short enhancement would only slightly impact our calculation of the average B_{scaled}, which takes an average of lobe field strength over the entire lobe crossing interval. We note it is also possible that our estimation of IMF orientation does not reflect the IMF orientation during MESSENGER's observations of the lobe field. MESSENGER is limited to single spacecraft observations, so measurements taken in the lobe and measurements taken in the IMF are separated in time by ~2 hr on average. However, IMF orientation can change significantly on the order of a few tens of minutes (James

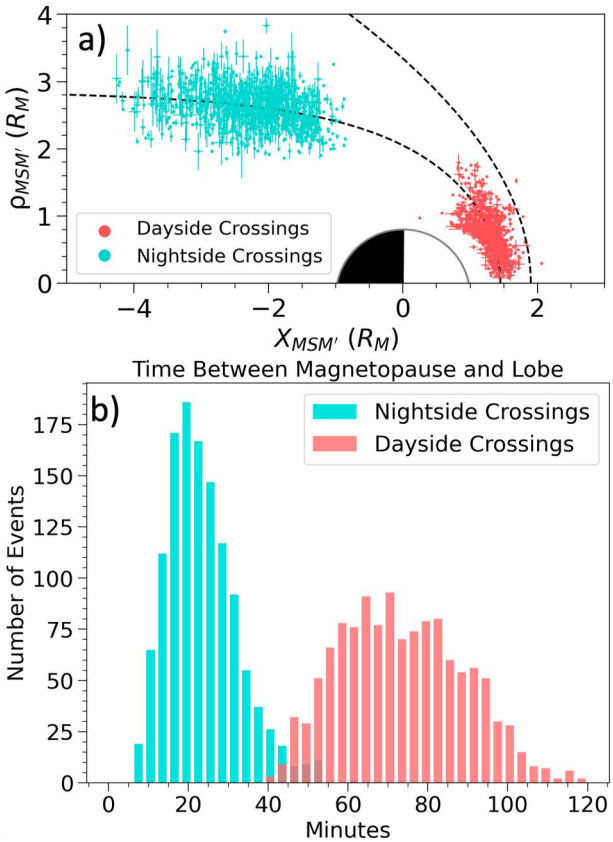


Figure 9. (a) Spatial distribution of 2,484 magnetopause crossings for 1,242 lobe magnetic field crossings detected by Mercury Surface, Space Environment, Geochemistry and Ranging in cylindrical coordinates (same as Figures 6e and 7b). Dayside ($X_{MSM'} > 0$) crossings are colored red, nightside ($X_{MSM'} < 0$) crossings are colored blue. The outer/inner dashed lines represent the nominal bowshock/magnetopause shape as determined by Shue et al. (1997) and Winslow et al. (2013). Error bars are the uncertainty in magnetopause position based on SBC2023. (b) The time between the center of the magnetopause crossings and the center of the lobe field detection for all 2,484 magnetopause. Dayside magnetopause crossings are again colored red, nightside magnetopause crossings are colored blue.

et al., 2017). The dual spacecraft of the BepiColombo mission will greatly shorten the time difference between upstream IMF measurements and the lobe field, at times providing simultaneous IMF and magnetotail measurements. Studies comparing lobe field strength to IMF orientation using BepiColombo will therefore allow for a more complete analysis of the impact of dayside magnetic reconnection rates on lobe magnetic flux by improving upstream IMF orientation estimates.

Next, we investigate the impact on magnetospheric compression on lobe field intensity. The spatial distribution of 2,484 (2 for each lobe detection) magnetopause crossings show a clear split between dayside ($X_{MSM'} > 0$) and nightside ($X_{MSM'} < 0$) crossings (Figure 9a). The duration between crossing the magnetopause and reaching the center of the lobe detection is influenced by the orbital trajectory and the position of the magnetopause (Figure 9b). The average time between MESSENGER crossing the center of a lobe field and the nightside magnetopause crossing was 24 min, while the average time between the center of the lobe field and dayside magnetopause crossing was 77 min. Next, we compute the average B_{scaled} value for all 1,242 lobe field detections and d for all 2,484 associated magnetopause crossings. Each lobe field encounter has an estimated average B_{scaled} which quantifies the relative strength of the lobe, as well as a nightside and dayside magnetopause d value which estimates the relative size of the magnetosphere compared to its nominal state along that same orbit. We plot the relationship B_{scaled} and d for each lobe field encounter, separating d for nightside and dayside magnetopause crossings in Figure 10. For both the nightside and dayside magnetopause crossings, we see a clear inverse relationship between B_{scaled} in the lobe and the associated d. This suggests that when the lobe field strength is enhanced ($B_{scaled} > 1$), then the magnetosphere tends to be compressed ($d < 0$), and when the lobe field strength is depleted ($B_{scaled} < 1$), the magnetosphere tends to be expanded ($d > 0$).

The magnetosphere of Mercury compresses and expands in response to the upstream dynamic pressure ($P_{dyn} = \rho_{sw} v^2$) of the solar wind (Ferraro, 1960; Sibeck et al., 1991; Slavin et al., 2021; Zhong et al., 2015), where ρ_{sw} is the solar wind mass density, and v is the solar wind velocity. Modeling studies have estimate nominal P_{dyn} values at Mercury's orbit average around 6–7 nPa (Fatemi et al., 2018), but vary greatly with heliocentric distance. Due to FIPS FOV constraints, the solar wind dynamic pressure cannot be reliably computed directly from plasma measurements. Instead, we derive P_{dyn} in the same methodology as Jia et al. (2019) and Slavin et al. (2014, 2019) in which we assume a pressure balance across the magnetopause boundaries and a negligible thermal pressure just inside (i.e., on the planetary side) of the magnetopause. In this idealized scenario, P_{dyn} is calculated via:

$$P_{dyn} = \frac{B_{MP}^2}{2\mu_0} * \left(0.88 \cos^2 \theta\right)^{-1} \quad [nPa] \tag{3}$$

Here, B_{MP} refers to the magnetic field strength just inside the magnetopause, μ_0 is the permeability of free space, and θ is the angle between the normal vector to the magnetopause and the solar wind velocity. The constant 0.88 was estimated via numerical gas modeling and acts as a drag coefficient as the plasma is diverted around the magnetopause (Spreiter et al., 1966). We estimate B_{MP} by averaging the magnetic field magnitude measurements for 5 min of MESSENGER observations on the planetary side of the inner boundary of the magnetopause crossings along all orbits in which we detect lobe magnetic field. To calculate θ, we measure the angle between the velocity of the solar wind (assumed to be radially outward from the Sun) and the normal vector to the closest point along the nominal magnetopause to the measured inner boundary of the magnetopause crossing. Equation 3 is most accurate for small (~<60°) values of θ, so we limit our P_{dyn} estimations for the dayside magnetopause

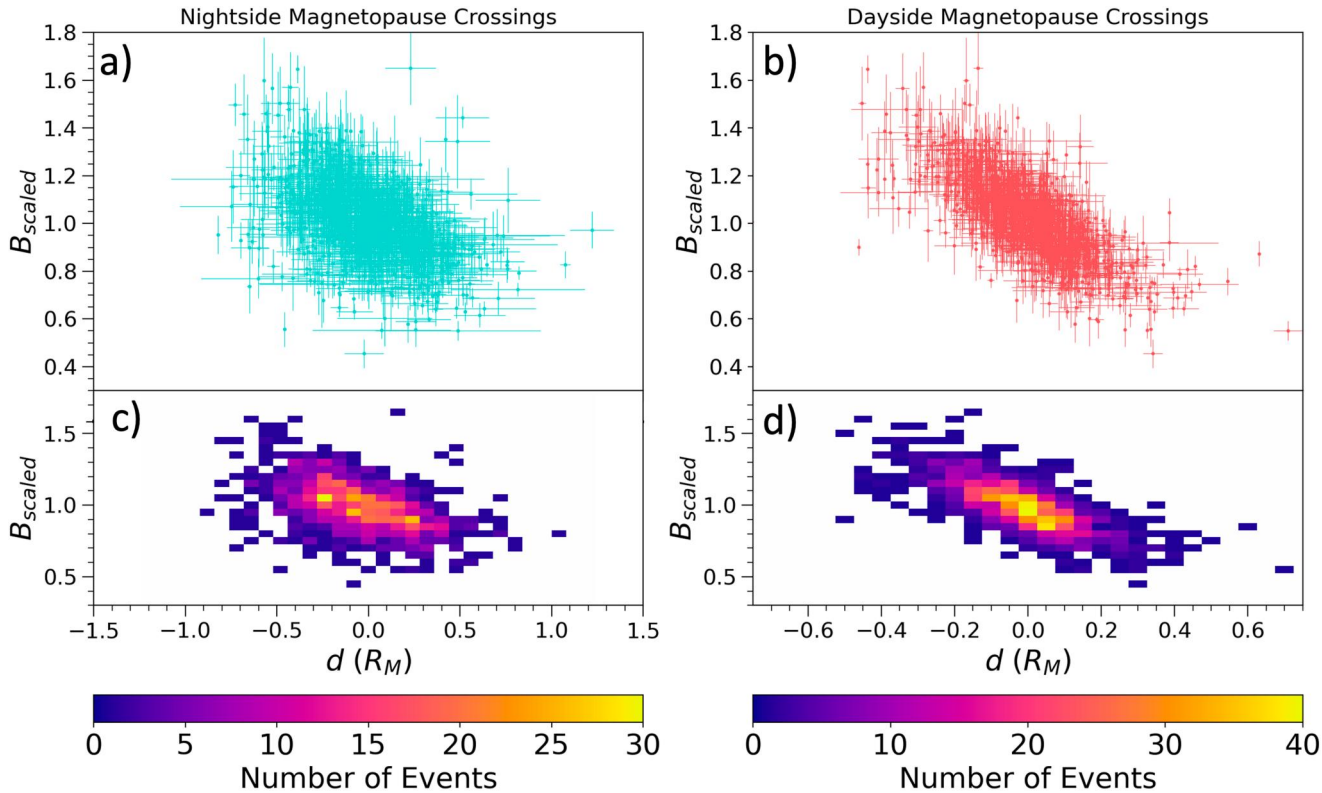


Figure 10. Average B_{scaled} for 1,242 lobe magnetic field detections versus distance from associated magnetopause crossing to nominal magnetopause boundary, d. d is calculated separately for magnetopause crossings that occur on the nightside ($X_{MSM'} < 0$) (a) and on the dayside ($X_{MSM'} > 0$) (b). Uncertainty in the average B_{scaled} is the standard deviation of the mean throughout the lobe magnetic field extent. Uncertainty in d is a result of the uncertainty in exact magnetopause location, taking d along a window of possible magnetopause crossings listed in SBC2023. Panels (c) and (d) are 30 × 30 binned color maps of panels (a) and (b), respectively, colored by the number of events that fall within each bin. Uncertainty in each measurement is not considered when constructing the color maps.

crossings. We note that we omit 1 lobe field detection that coincided with an extreme solar wind dynamic pressure estimate of >100 nPa.

The pressure in the magnetotail lobe is dominated by magnetic pressure, P_B, which is proportional to B^2_{lobe} ($P_B = \frac{B^2_{lobe}}{2\mu_0}$). Figure 11 plots the relationship between the average B_{scaled} and associated $\sqrt{P_{dyn}}$ estimate for all 1,242 lobe magnetic field crossings. For moderate dynamic pressure values (4.4 nPa < P_{dyn} < 14.4 nPa), there is a linear relationship between B_{scaled} and $\sqrt{P_{dyn}}$. When P_{dyn} > 14.4 nPa ($\sqrt{P_{dyn}}$ > 3.8 nPa$^{0.5}$) there is no longer a significant correlation between B_{scaled} and $\sqrt{P_{dyn}}$ (p-value = 0.2). Similarly, when P_{dyn} < 4.4 nPa ($\sqrt{P_{dyn}}$ < 2.2 nPa$^{0.5}$) there is no longer a significant correlation between B_{scaled} and $\sqrt{P_{dyn}}$ (p-value = 0.14). As a result, the expression for the relationship between B_{scaled} and $\sqrt{P_{dyn}}$ is limited to these nominal dynamic pressure conditions in between the dashed vertical lines in Figure 11:

$$B_{scaled} = (0.16 \pm 0.03)\sqrt{P_{dyn}} + (0.5 \pm 0.1) \tag{4}$$

Solving for P_{dyn}:

$$P_{dyn} = \left[\frac{B_{scaled} - (0.5 \pm 0.1)}{0.16 \pm 0.03}\right]^2 \tag{5}$$

We emphasize that this linear fit is only valid under moderate P_{dyn} conditions. In terms of B_{scaled}, Equation 5 is therefore only valid for when (0.69 < B_{scaled} < 1.2).

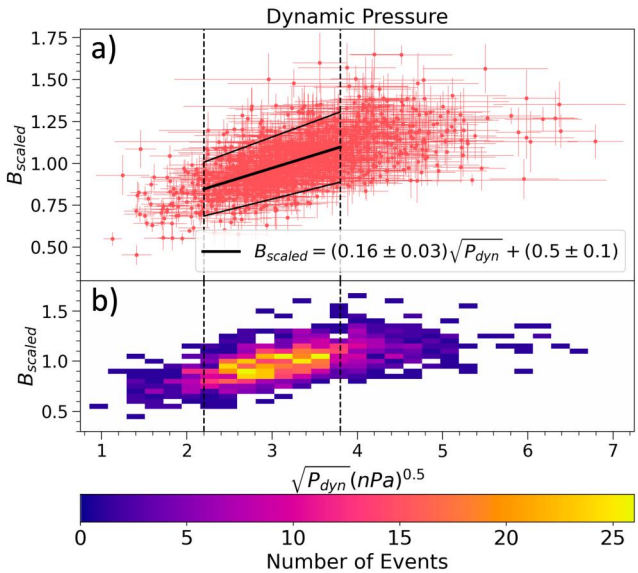


Figure 11. (a) Average B_{scaled} for 1,242 lobe magnetic field detections versus $\sqrt{P_{dyn}}$ from associated dayside ($X_{MSM'} > 0$) magnetopause crossings. Uncertainty in the average B_{scaled} is the standard deviation of the mean throughout the lobe magnetic field extent. Uncertainty in P_{dyn} is the standard deviation of the mean of the B_{MP} measurements. The center solid black line represents the equation of fit, with the uncertainties in the fit represented as the thinner dashed lines above and below. The dashed vertical lines represent the moderate dynamic pressure conditions under which the expression is valid (2.2 $nPa^{0.5}$ < $\sqrt{P_{dyn}}$ < 3.8 $nPa^{0.5}$).

Equations 4 and 5 demonstrate that average magnetic pressure in the lobe is directly correlated to the upstream dynamic pressure in the solar wind under moderate conditions for P_{dyn}. This expression could be used to estimate upstream solar wind dynamic pressure from average B_{scaled} throughout a lobe traversal. However, the uncertainties in the coefficients of the expression lead to imprecise estimations. Interestingly, B_{scaled} is no longer correlated with P_{dyn} under both very low (P_{dyn} < 4.4 nPa) and very high (P_{dyn} > 14.4 nPa) dynamic pressure conditions. Very low P_{dyn} are correlated to low Mach-number conditions, which may lead to the development of Alfvén wings on the nightside of Mercury (Sarantos & Slavin, 2009). This is thought occur under extreme solar wind conditions at Earth (Kivelson & Khurana, 2002) and consistently at Ganymede (Jia et al., 2008). Under these conditions, we would not expect lobe magnetic flux to behave in the same manner as in the nominal super-Alfvénic regime. Furthermore, under very high P_{dyn}, B_{scaled} no longer increases with increasing dynamic pressure estimates. This suggests the lobe flux may reach a maximal state, above which increasing dynamic pressure may be balanced by induction currents on the dayside, thermal heating of the plasma, or plasma entry into the system.

In summary, we did not find a significant correlation between our estimated $BZ_{MSM'}$ component of the IMF and B_{scaled}, as suggested by Slavin et al. (2012) based on four flybys of Mercury. Dayside magnetic reconnection leads to a brief period of approximately 3 min during which the lobe field intensity is enhanced before nightside reconnection begins, closing magnetic flux from the lobe and completing a Dungey cycle, ultimately restoring the lobe to its background intensity (Imber & Slavin, 2017). We posit that this short time scale of the Dungey cycle at Mercury ensures that dayside magnetic reconnection does not significantly impact the average lobe field intensity (B_{scaled}) across the extent of the lobe in most cases. However, we did observe a direct relationship between B_{scaled} and P_{dyn}, indicating that orbit-to-orbit variability in lobe magnetic field intensity is directly influenced by upstream solar wind dynamic pressure. This relationship is direct evidence of pressure balance across the nightside magnetosphere in which enhanced solar wind dynamic pressure acts inwardly on the magnetotail which is balanced by magnetic pressure supplied by the lobe magnetic field. We note that P_{dyn} is not the only variable impacting dayside magnetospheric volume. Chen et al. (2023) demonstrated that the dayside magnetopause location moves slightly planet-ward under negative IMF *BZ* conditions compared to positive IMF *BZ* conditions. However (Chen et al., 2023), also noted that P_{dyn} has a much stronger influence on magnetopause location compared to IMF *BZ*. Similarly, our results suggest average lobe field variability on orbit-to-orbit timescales also varies more with P_{dyn} than with IMF *BZ*.

4. Discussion

We have identified and analyzed the southern magnetotail lobe of Mercury through the magnetic field and plasma measurements obtained throughout MESSENGER's orbital mission. Using our lobe field identification method, we identify a total of 684 hr of lobe field observations along 1,242 MESSENGER orbits. From these data we determine the expression for the average lobe field intensity fall off with radial distance downtail for Mercury (Equation 1). This expression is useful for characterizing deviations from the nominal lobe field conditions, which could be indicative of active magnetic flux loading in the tail from dayside magnetic reconnection and/or magnetospheric compressions.

To investigate lobe field behavior at other planets, we compare Equation 1 to lobe field fall-off expressions derived at Earth (Fairfield & Jones, 1996), Jupiter (Kivelson & Khurana, 2002) and Saturn (Jackman & Arridge, 2011). Each expression follows the functional form $B_{lobe}(r) = Cr^{-\alpha} + b$ where r is radial distance downtail in planetary radii. Table 1 shows the derived coefficients to this expression for each of the planets listed above. The power of this expression, α, increases (becomes less negative) with heliocentric distance. Furthermore, the asymptote, b, is larger at Mercury compared to Earth and is negligible within the range sampled at

Table 1
Table of Lobe Field Fall-Off Properties at Mercury, Earth, Jupiter, and Saturn

$B_{lobe} = Cr^{-\alpha} + b$	Mercury	Earth	Jupiter	Saturn
C	135	1,659.2	2,900	251
α	−2.1	−1.46	−1.37	−1.20
b	31	7.5	0	0
Downtail sample range	1.4–4.7 R_M	15–150 R_E	30–150 R_J	18–70 R_S
Magnetopause standoff	1.45 R_M	10 R_E	75 R_J	25 R_S
Heliocentric distance (d_S [AU])	[0.31–0.47]	1.0	5.2	9.5

Note. Lobe fall-off follows the expression $B_{lobe} = Cr^{-\alpha} + b$ where r is the radial distance downtail in planetary radii. First three rows of the table these coefficients derived at Mercury (Equation 1), Earth (Fairfield & Jones, 1996), Jupiter (Kivelson & Khurana, 2002), and Saturn (Jackman & Arridge, 2011). Fourth row shows the distance downtail sampled in each of the studies to derive the lobe fall-off expression. Fifth row shows the magnetopause standoff distance for each planet determined at Mercury (Winslow et al., 2013), Earth (Mead, 1964), Jupiter (Joy et al., 2002) and Saturn (Achilleos et al., 2008). Sixth row shows mean heliocentric distance.

Jupiter and Saturn. To compare the lobe fall-off at these planets further, we plot the lobe fall-off expression as a function of planetary radii in Figure 12a. The extent of each of these curves is determined by the downtail orbital coverage assessed in each of these studies.

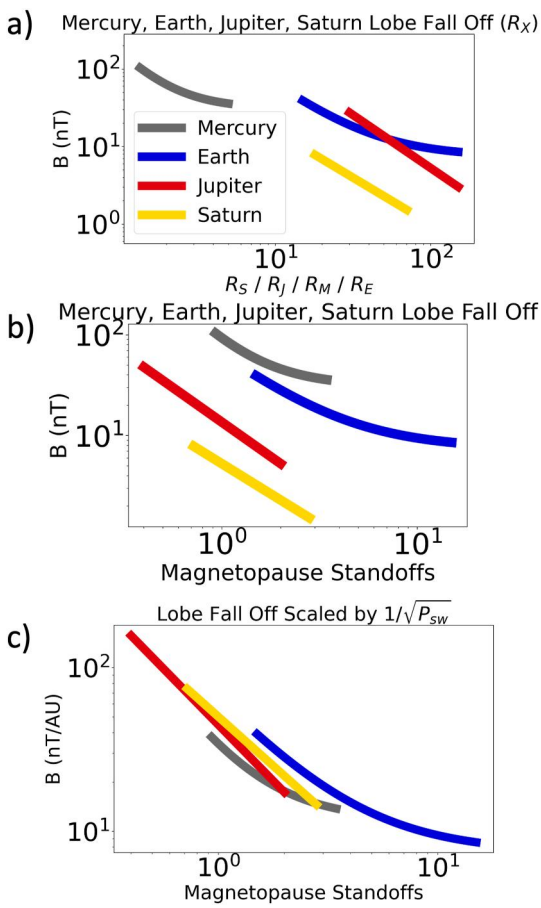


Figure 12. (a) B_{lobe} versus planetary radii comparison between Mercury (Equation 1), Earth (Fairfield & Jones, 1996), Jupiter (Kivelson & Khurana, 2002) and Saturn (Jackman & Arridge, 2011). (b) B_{lobe} versus magnetopause standoff distance. (c) B_{lobe} versus magnetopause standoff distance scaled by $\sqrt{P_{dyn}}$ estimated at the respective heliocentric distance.

Next, we scale the horizontal axis of Figure 12a to the respective magnetopause standoff distance at each planet listed in Table 1. In this manner, we are scaling each of the lobe field fall-off assessments to the size of the magnetosphere of their respective planets. For example, the coverage at Earth (Fairfield & Jones, 1996) extended to 15 times the nominal magnetopause standoff distance, whereas that at Jupiter and Saturn (Jackman & Arridge, 2011; Kivelson & Khurana, 2002) was only two times the standoff. Interestingly, we see that the strength of the lobe magnetic field at a given relative magnetopause standoff is inversely proportional to heliocentric distance (Figure 12b). For example, at two magnetopause standoffs, the lobe magnetic field strength is the highest at Mercury (44 nT), followed by Earth (28 nT), Jupiter (5 nT), and Saturn (2 nT).

In Section 3.4, we illustrated the linear relationship between $\sqrt{P_{dyn}}$ and B_{scaled} in Figure 11. To investigate this relationship in comparison to lobe fields at Earth, Jupiter, and Saturn, we estimate the nominal solar wind dynamic pressure at each planet, scaled to the solar wind dynamic pressure at Earth. We assume solar wind velocity, v, is constant throughout the heliosphere, and solar wind density, $n_{sw} \propto 1/d_S^2$, where d_S is the distance from the planet to the Sun. Therefore, $B_{lobe} \propto \sqrt{P_{dyn}} \propto 1/d_S$. In this manner, we scale each lobe field expression to the dynamic pressure conditions at Earth by dividing $B_{lobe}(r)$ by d_S in AU (Table 1). When scaled by d_S, the values for B_{lobe} across all four planets are quite similar at a given magnetopause standoff distance downtail (Figure 12c). This similarity is somewhat surprising given the large disparities in dipole magnetic field strengths across each of these planets. For example, the dipole field strength at Jupiter is ≈1,400 times that at Mercury (Anderson et al., 2011; Connerney et al., 2018). Relative to the size of the magnetosphere, the strength of the magnetotail lobe scales more with surrounding solar wind dynamic pressure than the dipole magnetic field strength of the planet. The similarity in relationship between lobe field strength and dynamic pressure may be useful for comparative magnetosphere studies that look to compare magnetospheric response to upstream solar wind conditions.

5. Summary

Here, we present an analysis of the southern magnetotail lobe of Mercury. From 3,332 MESSENGER orbits, we identify 1,242 lobe magnetic field intervals using based on FIPS and MAG measurements onboard MESSENGER. Based on magnetic field data within these intervals, we derive a new expression for the average fall-off of Mercury's lobe field strength with distance downtail: $B_{lobe}(r) = (135 \pm 8) * r^{(-2.1 \pm 0.3)} + (31 \pm 8)$. The rate of lobe field fall-off with radial distance does not change significantly under positive/negative IMF *BZ* conditions. We use this expression as a baseline to assess the extent to which each lobe crossing event is enhanced or diminished compared to its nominal state. Within the lobe crossings in our data set, we see evidence for both short timescale (2–3 min) fluctuations in magnetic field strength, as well as orbit-to-orbit timescale field strength variability. We do not see a significant correlation between average lobe field strength and the estimated upstream $Z_{MSM'}$ component of the IMF. However, we do not claim that IMF *BZ* has not effect on lobe field strength, but instead that this effect must be short lived due to the short Dungey cycle of Mercury, resulting in a lack of a significant correlation between the average lobe field properties and IMF orientation. However, we do find an inverse correlation between the volume of the magnetosphere (i.e., state of compression/expansion of the magnetopause boundaries) and the relative average magnetic field strength in the lobe field. Furthermore, we see a linear relationship between the estimated square root of solar wind dynamic pressure and the relative strength in the magnetotail lobes for moderate dynamic pressure conditions, suggesting the orbit-to-orbit variability in lobe field strength is attributable to upstream dynamic pressure conditions. Therefore, our results provide direct evidence for pressure balance between the magnetic pressure provided by magnetotail lobes and solar wind dynamic pressure acting inwardly on the magnetopause.

Data Availability Statement

In accordance with the AGU data policy, MESSENGER data are publicly available through the Planetary Plasma Interactions Node of the Planetary Data System (https://pds-ppi.igpp.ucla.edu/). The updated list of bowshock and boundary crossings reported in Sun et al. (2020) is included in the Zenodo repository (https://zenodo.org/record/8298647; Sun, 2023).

Acknowledgments
CFB is supported by the Irish Research Council Laureate Consolidator Grant (SOLMEX) awarded to CMJ. WS is supported by NASA Discovery Data Analysis Program Grant 80NSSC22K1061 and the National Science Foundation under Grant 2321595. MH is supported by the Discovery programme of the European Space Agency (Contract No: 4000137683/22/NL/GLC/my) and by the Science Foundation Ireland Grant 18/FRL/6199.

References

Achilleos, N., Arridge, C., Bertucci, C., Jackman, C., Dougherty, M., Khurana, K., & Russell, C. (2008). Large-scale dynamics of Saturn's magnetopause: Observations by Cassini. *Journal of Geophysical Research*, *113*(A11), A11209. https://doi.org/10.1029/2008ja013265

Aizawa, S., Griton, L. S., Fatemi, S., Exner, W., Deca, J., Pantellini, F., et al. (2021). Cross-comparison of global simulation models applied to Mercury's dayside magnetosphere. *Planetary and Space Science*, *198*, 105176. https://doi.org/10.1016/j.pss.2021.105176

Anderson, B. J., Acuña, M. H., Lohr, D. A., Scheifele, J., Raval, A., Korth, H., & Slavin, J. A. (2007). The magnetometer instrument on MESSENGER. In *The MESSENGER mission to Mercury* (pp. 417–450).

Anderson, B. J., Johnson, C. L., Korth, H., Purucker, M. E., Winslow, R. M., Slavin, J. A., et al. (2011). The global magnetic field of Mercury from MESSENGER orbital observations. *Science*, *333*(6051), 1859–1862. https://doi.org/10.1126/science.1211001

Andrews, G., Zurbuchen, T., Mauk, B., Malcom, H., Fisk, L. A., Gloeckler, G., et al. (2007). The energetic particle and plasma spectrometer instrument on the MESSENGER spacecraft. *Space Science Reviews*, *131*(1–4), 523–556. https://doi.org/10.1007/s11214-007-9272-5

Benkhoff, J., Murakami, G., Baumjohann, W., Besse, S., Bunce, E., Casale, M., et al. (2021). BepiColombo-mission overview and science goals. *Space Science Reviews*, *217*(8), 90. https://doi.org/10.1007/s11214-021-00861-4

Bevington, P. R., & Robinson, D. K. (2003). *Data reduction and error analysis for the physical sciences* (3rd ed.). McGraw-Hill.

Caan, M. N., McPherron, R. L., & Russell, C. T. (1973). Solar wind and substorm-elated changes in the lobes of the geomagnetic tail. *Journal of Geophysical Research (1896–1977)*, *78*(34), 8087–8096. https://doi.org/10.1029/ja078i034p08087

Chen, Y., Shue, J.-H., Zhong, J., & Shen, H.-W. (2023). Anomalous response of Mercury's magnetosphere to solar wind compression: Comparison to Earth. *The Astrophysical Journal*, *957*(1), 26. https://doi.org/10.3847/1538-4357/acf655

Chen, Y., Tóth, G., Jia, X., Slavin, J. A., Sun, W., Markidis, S., et al. (2019). Studying dawn-dusk asymmetries of Mercury's magnetotail using MHD-EPIC simulations. *Journal of Geophysical Research: Space Physics*, *124*(11), 8954–8973. https://doi.org/10.1029/2019ja026840

Collier, M. R., Slavin, J. A., Lepping, R. P., Ogilvie, K., Szabo, A., Laakso, H., & Taguchi, S. (1998). Multispacecraft observations of sudden impulses in the magnetotail caused by solar wind pressure discontinuities: Wind and IMP 8. *Journal of Geophysical Research*, *103*(A8), 17293–17305. https://doi.org/10.1029/97ja02870

Connerney, J., Kotsiaros, S., Oliversen, R., Espley, J., Joergensen, J. L., Joergensen, P., et al. (2018). A new model of Jupiter's magnetic field from Juno's first nine orbits. *Geophysical Research Letters*, *45*(6), 2590–2596. https://doi.org/10.1002/2018gl077312

DiBraccio, G. A., Slavin, J. A., Boardsen, S. A., Anderson, B. J., Korth, H., Zurbuchen, T. H., et al. (2013). MESSENGER observations of magnetopause structure and dynamics at Mercury. *Journal of Geophysical Research: Space Physics*, *118*(3), 997–1008. https://doi.org/10.1002/jgra.50123

DiBraccio, G. A., Slavin, J. A., Raines, J. M., Gershman, D. J., Tracy, P. J., Boardsen, S. A., et al. (2015). First observations of Mercury's plasma mantle by MESSENGER. *Geophysical Research Letters*, *42*(22), 9666–9675. https://doi.org/10.1002/2015gl065805

Exner, W., Heyner, D., Liuzzo, L., Motschmann, U., Shiota, D., Kusano, K., & Shibayama, T. (2018). Coronal mass ejection hits Mercury: AIKEF hybrid-code results compared to MESSENGER data. *Planetary and Space Science*, *153*, 89–99. https://doi.org/10.1016/j.pss.2017.12.016

Exner, W., Simon, S., Heyner, D., & Motschmann, U. (2020). Influence of Mercury's exosphere on the structure of the magnetosphere. *Journal of Geophysical Research: Space Physics*, *125*(7), e2019JA027691. https://doi.org/10.1029/2019ja027691

Fairfield, D. H., & Jones, J. (1996). Variability of the tail lobe field strength. *Journal of Geophysical Research*, *101*(A4), 7785–7791. https://doi.org/10.1029/95ja03713

Fatemi, S., Poirier, N., Holmström, M., Lindkvist, J., Wieser, M., & Barabash, S. (2018). A modelling approach to infer the solar wind dynamic pressure from magnetic field observations inside Mercury's magnetosphere. *Astronomy & Astrophysics*, *614*, A132. https://doi.org/10.1051/0004-6361/201832764

Fatemi, S., Poppe, A. R., & Barabash, S. (2020). Hybrid simulations of solar wind proton precipitation to the surface of Mercury. *Journal of Geophysical Research: Space Physics*, *125*(4), e2019JA027706. https://doi.org/10.1029/2019ja027706

Ferraro, V. C. A. (1960). An approximate method of estimating the size and shape of the stationary hollow carved out in a neutral ionized stream of corpuscles impinging on the geomagnetic field. *Journal of Geophysical Research (1896–1977)*, *65*(12), 3951–3953. https://doi.org/10.1029/jz065i012p03951

Gershman, D. J., Slavin, J. A., Raines, J. M., Zurbuchen, T. H., Anderson, B. J., Korth, H., et al. (2013). Magnetic flux pileup and plasma depletion in Mercury's subsolar magnetosheath. *Journal of Geophysical Research: Space Physics*, *118*(11), 7181–7199. https://doi.org/10.1002/2013ja019244

He, M., Vogt, J., Heyner, D., & Zhong, J. (2017). Solar wind controls on Mercury's magnetospheric cusp. *Journal of Geophysical Research: Space Physics*, *122*(6), 6150–6164. https://doi.org/10.1002/2016ja023687

Imber, S. M., & Slavin, J. A. (2017). MESSENGER observations of magnetotail loading and unloading: Implications for substorms at Mercury. *Journal of Geophysical Research: Space Physics*, *122*(11), 11402–11412. https://doi.org/10.1002/2017ja024332

Jackman, C. M., & Arridge, C. S. (2011). Statistical properties of the magnetic field in the Kronian magnetotail lobes and current sheet. *Journal of Geophysical Research*, *116*(A5), A05224. https://doi.org/10.1029/2010ja015973

James, M. K., Imber, S. M., Bunce, E. J., Yeoman, T. K., Lockwood, M., Owens, M. J., & Slavin, J. A. (2017). Interplanetary magnetic field properties and variability near Mercury's orbit. *Journal of Geophysical Research: Space Physics*, *122*(8), 7907–7924. https://doi.org/10.1002/2017ja024435

Jasinski, J. M., Slavin, J. A., Raines, J. M., & DiBraccio, G. A. (2017). Mercury's solar wind interaction as characterized by magnetospheric plasma mantle observations with MESSENGER. *Journal of Geophysical Research: Space Physics*, *122*(12), 12153–12169. https://doi.org/10.1002/2017ja024594

Jia, X., Slavin, J. A., Poh, G., DiBraccio, G. A., Toth, G., Chen, Y., et al. (2019). MESSENGER observations and global simulations of highly compressed magnetosphere events at Mercury. *Journal of Geophysical Research: Space Physics*, *124*(1), 229–247. https://doi.org/10.1029/2018ja026166

Jia, X., Walker, R. J., Kivelson, M. G., Khurana, K. K., & Linker, J. A. (2008). Three-dimensional MHD simulations of Ganymede's magnetosphere. *Journal of Geophysical Research*, *113*(A6), A06212. https://doi.org/10.1029/2007ja012748

Johnson, C. L., Philpott, L. C., Anderson, B. J., Korth, H., Hauck, S. A., Heyner, D., et al. (2016). MESSENGER observations of induced magnetic fields in Mercury's core. *Geophysical Research Letters*, *43*(6), 2436–2444. https://doi.org/10.1002/2015gl067370

Johnson, C. L., Purucker, M. E., Korth, H., Anderson, B. J., Winslow, R. M., Al Asad, M. M. H., et al. (2012). MESSENGER observations of Mercury's magnetic field structure. *Journal of Geophysical Research*, *117*(E12), E00L14. https://doi.org/10.1029/2012je004217

Joy, S. P., Kivelson, M. G., Walker, R. J., Khurana, K. K., Russell, C. T., & Ogino, T. (2002). Probabilistic models of the Jovian magnetopause and bow shock locations. *Journal of Geophysical Research*, *107*(A10), SMP17-1–SMP17-17. https://doi.org/10.1029/2001ja009146

Kivelson, M. G., & Khurana, K. K. (2002). Properties of the magnetic field in the Jovian magnetotail. *Journal of Geophysical Research*, *107*(A8), SMP23-1–SMP23-9. https://doi.org/10.1029/2001ja000249

Korth, H., Anderson, B. J., Gershman, D. J., Raines, J. M., Slavin, J. A., Zurbuchen, T. H., et al. (2014). Plasma distribution in Mercury's magnetosphere derived from MESSENGER magnetometer and fast imaging plasma spectrometer observations. *Journal of Geophysical Research: Space Physics*, *119*(4), 2917–2932. https://doi.org/10.1002/2013ja019567

Korth, H., Johnson, C. L., Philpott, L., Tsyganenko, N. A., & Anderson, B. J. (2017). A dynamic model of Mercury's magnetospheric magnetic field. *Geophysical Research Letters*, *44*(20), 10147–10154. https://doi.org/10.1002/2017gl074699

Korth, H., Tsyganenko, N. A., Johnson, C. L., Philpott, L. C., Anderson, B. J., Al Asad, M. M., et al. (2015). Modular model for Mercury's magnetospheric magnetic field confined within the average observed magnetopause. *Journal of Geophysical Research: Space Physics*, *120*(6), 4503–4518. https://doi.org/10.1002/2015ja021022

Lavorenti, F., Henri, P., Califano, F., Deca, J., Aizawa, S., André, N., & Benkhoff, J. (2022). Electron dynamics in small magnetospheres-insights from global, fully kinetic plasma simulations of the planet Mercury. *Astronomy & Astrophysics*, *664*, A133. https://doi.org/10.1051/0004-6361/202243911

Li, C., Jia, X., Chen, Y., Toth, G., Zhou, H., Slavin, J. A., et al. (2023). Global hall MHD simulations of Mercury's magnetopause dynamics and FTEs under different solar wind and IMF conditions. *Journal of Geophysical Research: Space Physics*, *128*(5), e2022JA031206. https://doi.org/10.1029/2022ja031206

Mead, G. D. (1964). Deformation of the geomagnetic field by the solar wind. *Journal of Geophysical Research (1896–1977)*, *69*(7), 1181–1195. https://doi.org/10.1029/jz069i007p01181

Milan, S., Cowley, S., Lester, M., Wright, D., Slavin, J., Fillingim, M., et al. (2004). Response of the magnetotail to changes in the open flux content of the magnetosphere. *Journal of Geophysical Research*, *109*(A4), A04220. https://doi.org/10.1029/2003ja010350

Milillo, A., Fujimoto, M., Murakami, G., Benkhoff, J., Zender, J., Aizawa, S., et al. (2020). Investigating Mercury's environment with the two-spacecraft BepiColombo Mission. *Space Science Reviews*, *216*(5), 1–78. https://doi.org/10.1007/s11214-020-00712-8

Nakai, H., Kamide, Y., & Russell, C. (1991). Influences of solar wind parameters and geomagnetic activity on the tail lobe magnetic field: A statistical study. *Journal of Geophysical Research*, *96*(A4), 5511–5523.

Petrinec, S. M., & Russell, C. T. (1996). Near-Earth magnetotail shape and size as determined from the magnetopause flaring angle. *Journal of Geophysical Research*, *101*(A1), 137–152. https://doi.org/10.1029/95ja02834

Poh, G., Slavin, J. A., Jia, X., Raines, J. M., Imber, S. M., Sun, W.-J., et al. (2017a). Coupling between Mercury and its nightside magnetosphere: Cross-tail current sheet asymmetry and substorm current wedge formation. *Journal of Geophysical Research: Space Physics*, *122*(8), 8419–8433. https://doi.org/10.1002/2017ja024266

Poh, G., Slavin, J. A., Jia, X., Raines, J. M., Imber, S. M., Sun, W.-J., et al. (2017b). Mercury's cross-tail current sheet: Structure, X-line location and stress balance. *Geophysical Research Letters*, *44*(2), 678–686. https://doi.org/10.1002/2016gl071612

Poh, G., Slavin, J. A., Jia, X., Sun, W.-J., Raines, J. M., Imber, S. M., et al. (2018). Transport of mass and energy in Mercury's plasma sheet. *Geophysical Research Letters*, *45*(22), 12163–12170. https://doi.org/10.1029/2018gl080601

Raines, J. M., Slavin, J. A., Zurbuchen, T. H., Gloeckler, G., Anderson, B. J., Baker, D. N., et al. (2011). MESSENGER observations of the plasma environment near Mercury. *Planetary and Space Science*, *59*(15), 2004–2015. (Mercury after the MESSENGER flybys). https://doi.org/10.1016/j.pss.2011.02.004

Romanelli, N., DiBraccio, G. A., Slavin, J., Bowers, C., & Weber, T. (2022). The search for magnetotail twisting at Mercury: Comparing MESSENGER observations with the terrestrial case. *Geophysical Research Letters*, *49*(24), e2022GL101643. https://doi.org/10.1029/2022gl101643

Rong, Z. J., Ding, Y., Slavin, J. A., Zhong, J., Poh, G., Sun, W. J., et al. (2018). The magnetic field structure of Mercury's magnetotail. *Journal of Geophysical Research: Space Physics*, *123*(1), 548–566. https://doi.org/10.1002/2017ja024923

Russell, C., Baker, D., & Slavin, J. (1988). The magnetosphere of Mercury. In *Mercury* (pp. 514–561). University of Arizona Press.

Sarantos, M., & Slavin, J. A. (2009). On the possible formation of Alfvén wings at Mercury during encounters with coronal mass ejections. *Geophysical Research Letters*, *36*(4), L04107. https://doi.org/10.1029/2008gl036747

Shue, J.-H., Chao, J. K., Fu, H. C., Russell, C. T., Song, P., Khurana, K. K., & Singer, H. J. (1997). A new functional form to study the solar wind control of the magnetopause size and shape. *Journal of Geophysical Research*, *102*(A5), 9497–9511. https://doi.org/10.1029/97ja00196

Sibeck, D. G., Lopez, R., & Roelof, E. C. (1991). Solar wind control of the magnetopause shape, location, and motion. *Journal of Geophysical Research*, *96*(A4), 5489–5495.

Siscoe, G., Ness, N., & Yeates, C. (1975). Substorms on Mercury? *Journal of Geophysical Research*, *80*(31), 4359–4363. https://doi.org/10.1029/ja080i031p04359

Slavin, J. A., Acuña, M. H., Anderson, B. J., Baker, D. N., Benna, M., Boardsen, S. A., et al. (2009). MESSENGER observations of magnetic reconnection in Mercury's magnetosphere. *Science*, *324*(5927), 606–610. https://doi.org/10.1126/science.1172011

Slavin, J. A., Anderson, B. J., Baker, D. N., Benna, M., Boardsen, S. A., Gloeckler, G., et al. (2010). MESSENGER observations of extreme loading and unloading of Mercury's magnetic tail. *Science*, *329*(5992), 665–668. https://doi.org/10.1126/science.1188067

Slavin, J. A., Anderson, B. J., Baker, D. N., Benna, M., Boardsen, S. A., Gold, R. E., et al. (2012). MESSENGER and Mariner 10 flyby observations of magnetotail structure and dynamics at Mercury. *Journal of Geophysical Research*, *117*(A1), 1215. https://doi.org/10.1029/2011ja016900

Slavin, J. A., DiBraccio, G. A., Gershman, D. J., Imber, S. M., Poh, G. K., Raines, J. M., et al. (2014). MESSENGER observations of Mercury's dayside magnetosphere under extreme solar wind conditions. *Journal of Geophysical Research: Space Physics*, *119*(10), 8087–8116. https://doi.org/10.1002/2014ja020319

Slavin, J. A., Imber, S. M., & Raines, J. M. (2021). A Dungey cycle in the life of Mercury's magnetosphere. In *Magnetospheres in the solar system* (pp. 535–556). American Geophysical Union (AGU).

Slavin, J. A., Middleton, H. R., Raines, J. M., Jia, X., Zhong, J., Sun, W.-J., et al. (2019). MESSENGER observations of disappearing dayside magnetosphere events at Mercury. *Journal of Geophysical Research: Space Physics*, *124*(8), 6613–6635. https://doi.org/10.1029/2019ja026892

Slavin, J. A., Owen, C. J., Dunlop, M. W., Borälv, E., Moldwin, M. B., Sibeck, D. G., et al. (2003). Cluster four spacecraft measurements of small traveling compression regions in the near-tail. *Geophysical Research Letters*, *30*(23), A07S20. https://doi.org/10.1029/2003gl018438

Slavin, J. A., Smith, E. J., Sibeck, D. G., Baker, D. N., Zwickl, R. D., & Akasofu, S.-I. (1985). An ISEE 3 study of average and substorm conditions in the distant Magnetotail. *Journal of Geophysical Research*, *90*(A11), 10875–10895. https://doi.org/10.1029/ja090ia11p10875

Slavin, J. A., Smith, M. F., Mazur, E. L., Baker, D. N., Iyemori, T., Singer, H. J., & Greenstadt, E. W. (1992). ISEE 3 plasmoid and TCR observations during an extended interval of substorm activity. *Geophysical Research Letters*, *19*(8), 825–828. https://doi.org/10.1029/92gl00394

Spreiter, J. R., Summers, A. L., & Alksne, A. Y. (1966). Hydromagnetic flow around the magnetosphere. *Planetary and Space Science*, *14*(3), 223–253. https://doi.org/10.1016/0032-0633(66)90124-3

Sun, W. J. (2023). Lists of magnetopause and bow shock crossings of Mercury by MESSENGER spacecraft. *Zenodo*. https://doi.org/10.5281/zenodo.8298647

Sun, W. J., Dewey, R. M., Aizawa, S., Huang, J., Slavin, J. A., Fu, S., et al. (2022). Review of Mercury's dynamic magnetosphere: Post-MESSENGER era and comparative magnetospheres. *Science China Earth Sciences*, *65*, 1–50. https://doi.org/10.1007/s11430-021-9828-0

Sun, W. J., Raines, J. M., Fu, S. Y., Slavin, J. A., Wei, Y., Poh, G. K., et al. (2017). MESSENGER observations of the energization and heating of protons in the near-Mercury Magnetotail. *Geophysical Research Letters*, *44*(16), 8149–8158. https://doi.org/10.1002/2017gl074276

Sun, W. J., Slavin, J. A., Smith, A. W., Dewey, R. M., Poh, G. K., Jia, X., et al. (2020). Flux transfer event showers at Mercury: Dependence on plasma β and magnetic shear and their contribution to the Dungey cycle. *Geophysical Research Letters*, *47*(21), e2020GL089784. https://doi.org/10.1029/2020gl089784

Trávníček, P. M., Schriver, D., Hellinger, P., Herčík, D., Anderson, B. J., Sarantos, M., & Slavin, J. A. (2010). Mercury's magnetosphere–solar wind interaction for northward and southward interplanetary magnetic field: Hybrid simulation results. *Icarus*, *209*(1), 11–22. https://doi.org/10.1016/j.icarus.2010.01.008

Winslow, R. M., Anderson, B. J., Johnson, C. L., Slavin, J. A., Korth, H., Purucker, M. E., et al. (2013). Mercury's magnetopause and bow shock from MESSENGER magnetometer observations. *Journal of Geophysical Research: Space Physics*, *118*(5), 2213–2227. https://doi.org/10.1002/jgra.50237

Winslow, R. M., Lugaz, N., Philpott, L., Farrugia, C. J., Johnson, C. L., Anderson, B. J., et al. (2020). Observations of extreme ICME ram pressure compressing Mercury's dayside magnetosphere to the surface. *The Astrophysical Journal*, *889*(2), 184. https://doi.org/10.3847/1538-4357/ab6170

Zhong, J., Wan, W. X., Wei, Y., Slavin, J. A., Raines, J. M., Rong, Z. J., et al. (2015). Compressibility of Mercury's dayside magnetosphere. *Geophysical Research Letters*, *42*(23), 10135–10139. https://doi.org/10.1002/2015gl067063